Journal of Medicinal Chemistry

Article

Linker Modification Strategies to Control the Prostate-specific Membrane Antigen (PSMA)-Targeting and Pharmacokinetic Properties of DOTA-Conjugated PSMA Inhibitors

Martina Benesova, Ulrike Bauder-Wüst, Martin Schäfer, Karel D. Klika, Walter Mier, Uwe Haberkorn, Klaus Kopka, and Matthias Eder

J. Med. Chem., **Just Accepted Manuscript** • DOI: 10.1021/acs.jmedchem.5b01210 • Publication Date (Web): 15 Feb 2016

ACS Publications

Journal of Medicinal Chemistry is published by the American Chemical Society. 1155 Sixteenth Street N.W., Washington, DC 20036

Linker Modification Strategies to Control the Prostate-specific Membrane Antigen (PSMA)-Targeting and Pharmacokinetic Properties of DOTA-Conjugated PSMA Inhibitors

Martina Benešová,[§] Ulrike Bauder-Wüst,[§] Martin Schäfer,[§] Karel D. Klika,[†] Walter Mier,[‡] Uwe Haberkorn,[‡,∥] Klaus Kopka,[§,⊥] and Matthias Eder*[,§,⊥]

[§]Division of Radiopharmaceutical Chemistry, German Cancer Research Center (DKFZ), Heidelberg, Germany

[†]Molecular Structure Analysis, German Cancer Research Center (DKFZ), Heidelberg, Germany

[‡]Department of Nuclear Medicine, University Hospital Heidelberg, Heidelberg, Germany

[∥]Clinical Cooperation Unit Nuclear Medicine, German Cancer Research Center (DKFZ), Heidelberg, Germany

Since prostate-specific membrane antigen (PSMA) is up-regulated in nearly all stages of prostate cancer (PCa), PSMA can be considered as a viable diagnostic biomarker and treatment target in PCa. This project is focused on the development and evaluation of a series of compounds

directed against PSMA. The modifications to the linker are designed to improve the binding potential and pharmacokinetics for theranostic application. In addition, the results help to further elucidate the structure–activity relationships (SAR) of the resulting PSMA inhibitors. Both *in vitro* and *in vivo* experiments of 18 synthesized PSMA inhibitor variants showed that systematic chemical modification of the linker has a significant impact on the tumor-targeting and pharmacokinetic properties. This approach can lead to an improved management of patients suffering from recurrent prostate cancer by the use of one radiolabeling precursor, which can be radiolabeled with either ^{68}Ga for diagnosis or with ^{177}Lu, or ^{225}Ac, for therapy.

KEYWORDS

Prostate cancer, prostate-specific membrane antigen (PSMA), low-molecular weight ligands, structure–activity relationships (SAR), PET imaging, endoradiotherapy, theranostics

INTRODUCTION

Prostate cancer (PCa) is the most commonly diagnosed malignancy in men worldwide and remains one of the leading causes for their cancer-related deaths.[1–3] Despite significant efforts, currently available diagnostic and therapeutic strategies are often ineffective,[4,5] particularly for hormone-refractory PCa resulting in a very poor prognosis for these patients.[6] With regard to this situation, further development of a biomarker-specific detection, accurate staging of primary as well as recurrent disease, and highly efficient endoradiotherapy are of utmost clinical interest.

Prostate-specific membrane antigen (PSMA) is a type II membrane glycoprotein with an extensive extracellular domain (44–750 amino acids) and plays a significant role in prostate carcinogenesis and progression.[7] For nearly two decades PSMA has been a well-characterized viable biomarker and treatment target in PCa.[8] Additionally, low-level PSMA expression was shown in primary renal tumors[9] and transitional cell carcinoma of the bladder.[10] Moreover, PSMA is presented on the neovasculature within multiple, non-prostate solid tumors and may also be a promising molecule for targeting tumor-associated blood vessels.[11,12]

Diverse chemical scaffolds have been investigated as potential ligands of PSMA including low-molecular weight inhibitors,[13–16] various generations of antibodies,[17–19] RNA aptamer conjugates,[20–22] and several combinations with targeted nanoparticles.[23–25] Originally, PSMA was identified as the antigen of the monoclonal antibody (mAB) 7E11-C5. Its ^{111}In-labelled version, commercially known as ProstaScint, is the only FDA (Food and Drug Administration) approved radiopharmaceutical for the PSMA-targeted treatment of PCa.[26,27] ^{111}In-Labeled ProstaScint recognizing the intracellular domain of PSMA became the most widely studied radiolabeled

PSMA-targeting mAB. However, the large size of this antibody tends to prolong clearance and access to all portions of the tumor is typically restricted, especially for viable cells with intact membranes.[28,29] A second generation genetically engineered humanized monoclonal antibody is huJ591, which recognizes the extracellular portion of PSMA and was recently successfully translated into clinical trials. ^{90}Y-, ^{111}In-, ^{131}I-, and ^{177}Lu-labeled huJ591[30,31] have all been described thus far. Another example of a successful candidate for clinical testing is ^{89}Zr-Df-IAB2M, an anti-PSMA minibody (Mb), for imaging primary prostate cancer and soft tissue and bone metastases.[32] Low-molecular weight PSMA-targeting radioligands[8,15,33–36] are also shown to detect metastatic or recurrent PCa with high specificity and sensitivity and seem to be more potent than antibodies with respect to tissue penetration, half-life of circulation, and production-related costs.

The active site of PSMA consists of a binuclear Zn^{2+} active site and the S1 and S1' subpockets. Besides the primary interactions of urea and carboxylate groups at the Zn^{2+} active site and the S1' subpocket of PSMA, there are potential lipophilic interactions within the S1-accessory hydrophobic pocket. Prospective compounds lacking any one of these interactions have shown significant attenuation in their binding properties.[37–42] However, the glutamate–urea–lysine binding structural motif is a building block well suited for preparing potent PSMA-inhibitors.[41,43]

In an attempt to improve both the detection by scintigraphic technologies such as positron emission tomography (PET) and the treatment of PCa by PSMA-targeting systemic radionuclide therapy (endoradiotherapy), we synthesized a series of urea-based DOTA-conjugated PSMA-inhibitors (Figure 1) and evaluated their *in vitro* and *in vivo* properties. To retain the binding affinity of the PSMA inhibitors, various linker moieties (Figure 2) were investigated between the pharmacophore and DOTA, introduced correspondingly as carboxamide, which is able to

incorporate diagnostic as well as therapeutic radionuclides. The relative ease of solid-phase synthesis also facilitates structure–activity relationship studies. Overall, our approach can serve as a useful platform for structure-aided design and further development of these inhibitors with favorable tumor-targeting and pharmacokinetic properties.[44]

RESULTS

The multistep solid-phase synthesis provided the compounds in isolated overall yields of 32–48%. Subsequent purification provided final products with purities >98% by analytical RP-HPLC. Analytical data for the compounds are presented in Table 1. All compounds were found to be stable for at least 6 months as lyophilized powders at −20 °C, and all compounds are stable for at least 3 months in d_6-DMSO solution at −20 °C with only slight decomposition evident after an extended period of time. However, at ambient temperature, compound stability is limited to less than 1 month in d_6-DMSO solution as confirmed by NMR spectroscopy, RP-HPLC, and MALDI-MS.

The PSMA inhibitors synthesized (Figure 2) were divided into four sets each based on the chemical similarities in the structural changes of the linker. The first set of compounds (**11–16**) included different numbers and arrangement of aromatic units (aminobenzyl) in the linker region. Compound **11** employs as a first building block linear aminohexanoic acid and then an aromatic amino acid (4-aminomethylbenzoic acid, AMBA). The linker in **12**, **13**, **14** and **15** contains either one, two, three or four AMBA building blocks, respectively. Additionally, **16** contains biphenyl-L-alanine as a linker. The second set of compounds (**17–20**), inclusive Glu-NH-CO-NH-Lys-2-naphthyl-L-Ala-cyclohexane-DOTA (commercially known as PSMA-617[44]), comprises 2-naphthyl-L-alanine as the first building block which is more flexible compared to aminobenzyl used in the first set. The cyclohexanoic acid creates the second building block in **17** (PSMA-617). Compound **18** differs in conformation as it employs 2-naphthyl-D-alanine. **19**, on the other hand, differs in the naphthylic structure as it uses 1-naphthyl-L-alanine. Moreover **20** demonstrates simple sequence interchange of the building blocks compared to **17**. The third set

of compounds (**21–24**) describes the influence of the second building block while maintaining the 2-naphthyl-L-alanine building block as a constant in the linker (**21**), while **22** contains additionally an aromatic unit, **23** aminohexanoic acid and **24** both an aromatic and cyclohexane unit. The fourth set of compounds (**25–28**) examines the influence of the cyclohexane moiety as the linker contains one cyclohexane ring (**25**), two cyclohexane rings (**26**) and three cyclohexane rings (**27**). Moreover, **28** employs one cyclohexane and one aromatic ring in the linker area.

Characterization of the compounds was conducted extensively by ^{1}H and ^{13}C NMR. Analysis of the compounds using 2D NMR techniques (COSY, HSQC, and HMBC spectra) to assign the signals from the 1D ^{1}H and ^{13}C NMR spectra was focused on compounds **12**, **14**, **17**, and **19** as these inhibitors represented the most promising candidates for success in concert with the stated aims of the work and the unequivocal assignment of signals was accomplished for these structures. Assignments could then be applied to the remaining compounds by analogy together with the use of incremental shift calculations to effect partial or tentative assignments. DEPT spectra were used for the assignment of the ^{13}C multiplicities but were also effective for the direct observation of solvent-overlapped signals. The dynamic effects arising from the slow motional averaging of the macrocyclic ring on the NMR timescale leading to severe broadening of signals in many cases, particularly those associated with the macrocyclic ring, were attenuated for ^{13}C NMR spectra by the acquisition at lower field and by the acquisition of spectra at elevated temperatures (generally 70 and 90 °C). All compounds were deemed to be fully consistent with their assigned structures by NMR in terms of proton count, carbon count, and carbon multiplicities. For NMR data and spectra, see Supporting Information.

Radiolabeling with ^{177}Lu (15 min at 98 °C) provided labeling efficiency >98% for all compounds, even for low amounts of used precursor (0.5 nmol). Radiolabeling with ^{68}Ga

provided labeling efficiencies >95% (5 nmol) or >90% for low amounts of precursor (0.5 nmol) after 15 min at 98 °C. However, **24** demonstrated instability and degradation at higher temperatures as confirmed by NMR and was thus neither tested *in vitro* nor *in vivo*.

The potential binding to the serum proteins was performed for seven selected compounds, viz. **11**, **14**, **17**, **22**, **26**, and **28**. These representative compounds tested through gel filtration did not demonstrate any transfer of activity to proteins contained in human serum. The distribution coefficients determined via distribution in a two-phase system (*n*-octanol and HEPES buffer at pH 7.4) are presented in Table 1. The log*D* values ranged from –2.12 ± 0.33 for **15** to –0.91 ± 0.49 for **25** ($p = 0.0005$). To compensate for differing solubilities, all compounds were diluted to 10 mM solution in DMSO for subsequent experiments.

All compounds revealed high inhibition potencies for PSMA for the human prostate cancer cell line LNCaP. In this library of 18 compounds, significant differences in PSMA inhibition potencies were found, e.g. $K_i = 0.50 \pm 0.63$ nM for **16** and 28.60 ± 13.10 nM for **21** ($p = 0.0206$). Four sets of compounds were defined with each set representing chemical structure related similarities. The first set is based on the different number and arrangement of aromatic rings in the linker area and demonstrated overall high inhibition potencies except for **11** ($K_i = 15.31 \pm 5.10$ nM). The linker area of this compound contains two building blocks, the first one is composed of aminohexanoic acid and the second one contains a benzene ring. The removal of the aminohexanoic acid led to the compound **12** with significantly improved binding affinity ($K_i = 1.97 \pm 0.76$ nM; $p = 0.0110$). The compounds with a contiguous line of an increasing number of aromatic rings, **13** ($K_i = 7.51 \pm 6.12$ nM), **14** ($K_i = 0.53 \pm 0.47$ nM), and **15** ($K_i = 6.19 \pm 1.51$ nM) showed fluctuation in their binding affinities. A high binding affinity was demonstrated also

by the final member of this set, **16**, with a biphenyl-L-alanine building block (K_i = 0.50 ± 0.63 nM).

The second set is based on different arrangements of the naphthyl alanine and the cyclohexane moiety. Compound **17** which contains 2-naphthyl-L-alanine and cyclohexane showed a K_i of 2.34 ± 2.94 nM, **18** with 2-naphthyl-D-alanine and cyclohexane demonstrated a K_i of 8.86 ± 3.64 nM, and **19** with 1-naphthyl-L-alanine and cyclohexane exhibited a K_i of 12.78 ± 6.41 nM. The last compound of this set, **20**, which also consists of 2-naphthyl-L-alanine and cyclohexane, however as an inverse arrangement as compared to **17**, showed the lowest binding affinity (K_i = 17.70 ± 1.41 nM; p = 0.0012).

The third set is characterized by having 2-naphthyl-L-alanine as a constant in the linker. Compound **21** with 2-naphthyl-L-alanine demonstrated the lowest binding affinity of all compounds (K_i = 28.60 ± 13.10 nM). When the second building block, a benzene ring (**22**) or aminohexanoic acid (**23**), was added, the binding affinity increased significantly (K_i = 1.81 ± 0.80 nM for **22**; p = 0.0241 and K_i = 6.31 ± 2.22 nM for **23**; p = 0.0439).

Finally, the last set is based on compounds with a contiguous line of an increasing number of cyclohexane moieties. No significant differences in binding affinity for these compounds were observed (K_i = 9.33 ± 28.39 nM for **25**; K_i = 20.96 ± 29.65 nM for **26**; K_i = 19.40 ± 5.18 nM for **27**). Compound **28** contains one cyclohexane and one additional aromatic moiety (a benzene ring) in the linker (K_i = 24.71 ± 24.99 nM).

In addition, the specific internalization into LNCaP cells was determined for all compounds synthesized in this study. The first set of compounds demonstrated overall high internalization

(5.11 ± 2.46 %IA/10^6 LNCaP cells for **12**; 3.66 ± 1.31 %IA/10^6 LNCaP cells for **13**; 12.49 ± 1.38 %IA/10^6 LNCaP cells for **14**; 6.86 ± 1.59 %IA/10^6 LNCaP cells for **15**) except for **11** (2.11 ± 0.02 %IA/10^6 LNCaP cells) and **16** (2.22 ± 1.01 %IA/10^6 LNCaP cells). These compounds with a contiguous line of an increasing number of aromatic rings, **12**, **13**, **14**, and **15**, showed fluctuation regarding their internalization into LNCaP cells. The optimal number of benzene rings in the linker based on binding affinity appears to be three aromatic moieties, as represented by **14**.

Compound **17** is the most promising compound of the second set based on the inhibitory potency, showing overall the highest internalization (16.17 ± 3.66 %IA/10^6 LNCaP cells). With more apparent changes in the linker area of **17**, the internalization strongly decreased (7.18 ± 3.47 %IA/10^6 LNCaP cells for **18**, 0.90 ± 0.07 %IA/10^6 LNCaP cells for **19**, 0.13 ± 0.01 %IA/10^6 LNCaP cells for **20**).

The third set of compounds revealed the importance for the presence of aromatic building blocks in the linker as **22** showed the highest internalization of this set (7.17 ± 2.82 %IA/10^6 LNCaP cells). Compounds **21** and **23** demonstrated similar internalization, 1.77 ± 1.19 %IA/10^6 LNCaP cells and 2.99 ± 1.65 %IA/10^6 LNCaP cells, respectively.

Finally, the last set of compounds exhibited very low internalization into LNCaP cells (1.24 ± 0.24 %IA/10^6 LNCaP cells for **25**, 1.43 ± 0.21 %IA/10^6 LNCaP cells for **26**, and 0.03 ± 0.02 %IA/10^6 LNCaP cells for **27**). The last compound of this set, **28**, with an additional aromatic moiety, showed higher internalization than the other members of this set, 2.70 ± 2.06 %IA/10^6 LNCaP cells. The results from the binding and internalization assays are summarized in Table 2.

For the overall cell surface binding and internalization (without subtracting the non-specific cell surface binding and the non-specific internalized fraction), see Supporting Information.

The time–activity curves obtained from μPET imaging of ^{68}Ga-labeled compounds in nude mice bearing LNCaP tumor xenografts resulted in SUV values of accumulated radioactivity in the tumor, muscle, and kidneys as well as for tumor-to-muscle (tumor-to-background, T-to-B) ratios at 1 h post-injection (Table 3). The highest T-to-B ratio (8.5) was demonstrated by **17** when SUV_{mean} for the tumor was 0.59 ± 0.32 and SUV_{mean} for the muscle was 0.07 ± 0.02. The uptake in the kidneys was low compared to other compounds (SUV_{mean} for the kidneys = 2.87 ± 0.66). The lowest T-to-B ratio (0.9) was demonstrated by **27** (SUV_{mean} for the tumor = 0.18 ± 0.07 and SUV_{mean} for the muscle = 0.21 ± 0.05). In general, the PET imaging properties were in an excellent agreement with the obtained internalization results *in vitro*. In the first set of compounds, the most promising one with the highest binding affinity and internalization, **14**, showed also one of the highest uptakes in the tumor and T-to-B ratio (SUV_{mean} for the tumor = 0.58 ± 0.20 and T-to-B ratio = 5.4). On the other hand, the less favorable compound on these parameters, **11**, demonstrated a T-to-B ratio of 3.8 while the SUV_{mean} for the tumor was 0.30 ± 0.09. In the second set of compounds, high tumor uptake was only found for **17** (SUV_{mean} for the tumor 0.59 ± 0.32) and **18** (SUV_{mean} for the tumor 0.69 ± 0.15), the former of which also showed the most favorable internalization in this set compared to **19** and **20** (SUV_{mean} for the tumor 0.29 ± 0.07 and 0.39 ± 0.07, respectively). In the third set of compounds, **22** exhibited the highest internalization and also the highest tumor uptake (SUV_{mean} for the tumor 0.52 ± 0.26) and the T-to-B ratio (5.2) in this set. The T-to-B ratio for **21** was 1.6 (SUV_{mean} for the tumor 0.31 ± 0.06) and for **23** 2.0 (SUV_{mean} for the tumor 0.14 ± 0.10). The last set of compounds (**25**–**27**) showed almost no internalization and also demonstrated low SUV_{mean} in the tumor as well as low T-to-B

ratios (SUV_{mean} for the tumor 0.23 ± 0.04, 0.30 ± 0.10, and 0.18 ± 0.07, respectively; T-to-B ratio 1.5, 2.3, and 0.9, respectively). However, **28** with higher internalization showed also higher tumor uptake (SUV_{mean} for the tumor 0.54 ± 0.16) and higher T-to-B ratio (3.9) compared to other compounds of this set. The graphic illustrations of the time–activity curves for each compound are stated in the Supplemental Information.

The *μ*PET images 2 hours post-injection revealed variable tumor visualization as well as clearance of the radiolabeled compounds from the kidneys and the whole body. The first set of compounds with generally high inhibition potency and internalization into LNCaP cells demonstrated good visualization of the tumor except for **11**. The *μ*PET imaging of the second set of compounds correlates highly with the *in vitro* properties. The best imaging potential was demonstrated by **17** and **18** which have also shown the highest internalization in this set. Compounds **19** and **20** exhibited very low tumor accumulation as well as almost no internalization. The *in vitro* assays also pointed to the most promising compound of the third set, **22**, which showed high *in vitro* binding affinity and internalization as well as high *in vivo* accumulation in the tumor. The last set of compounds (**25**–**28**) with the overall worst *in vitro* properties exhibited also the worst *in vivo* imaging properties. The *μ*PET coronal slices are depicted in Figure 3 for the first set of ^{68}Ga-labeled compounds (**11**–**16**), in Figure 4 for the second set (**17**–**20**), in Figure 5 for the third set (**21**–**23**), and in Figure 6 for the fourth set (**25**–**28**), all 2 hours post-injection. The *in vivo* distribution is additionally demonstrated by the respective maximum intensity projections (MIP). All *μ*PET images for each time point (20, 40, 60 and 120 min p.i.) are presented in the Supplemental Information.

DISCUSSION AND CONCLUSIONS

In this study, we evaluated the effect of modifying the hydrophobic linker moiety between the glutamate–urea–lysine binding motif and the DOTA chelator. DOTA is a chelating agent applicable predominantly for the complexation of trivalent metal cations, which includes the clinically relevant radiometals ^{44}Sc, ^{68}Ga, and ^{86}Y for PET; ^{67}Ga and ^{111}In for SPECT; ^{90}Y and ^{177}Lu for beta therapy; and ^{213}Bi and ^{225}Ac for alpha therapy. The intentionally small library of PSMA inhibitors prepared here provides a promising tool for the targeting and optimal detection, staging, and treatment of prostate cancer, resulting in the improved management of patients suffering from prostate cancer.

The most commonly used radiopharmaceutical for PET by far is 2-deoxy-2-[^{18}F]fluoro-D-glucose ([^{18}F]FDG). FDG-PET can be used for the diagnosis and therapy response monitoring of many types of cancers, but it is not effective for most primary prostate tumors and metastases due to the low glycolytic rate of prostate cancer.[45–47] Both androgen-sensitive and androgen-independent prostate tumors have shown higher ^{11}C- or ^{18}F-choline uptake than that with ^{18}F-FDG. However, the detection rate with choline, especially at a PSA below 1 ng/mL, is still low.[48–50] As a result, there has been a sustained effort for the development of radiolabeled peptides/peptidomimetics[13,15,16] and anti-PSMA monoclonal antibodies (mAb).[51–53]

In contrast to previous approaches, several groups have designed low-molecular weight inhibitors of PSMA with binding affinities similar to that of huJ591, but possessing faster accumulation uptake rates by tumor tissue and with faster background clearance. The DOTA-conjugated PSMA inhibitors **11** to **28** described here can potentially be used as PET tracers after radiolabeling with the readily available generator-produced positron emitter ^{68}Ga, and, after

radiolabeling with particle emitters such as ^{177}Lu and ^{225}Ac, also as therapeutic radiopharmaceuticals for endoradiotherapy of prostate cancer. This aimed-at theranostic approach represents the main rationale for the work described here.

Thus, structural features of the enzymatic binding pocket of PSMA were used for the design of a rational inhibitor. The pocket has a strong preference for P1 acidic residues, e.g., Asp and Glu, and therefore the pharmacophore was proposed to present three invariant carboxylic groups able to interact with the respective S1 and S1' pockets. In addition, the carbonyl oxygen of the urea function coordinates to the Zn^{2+} active site. Besides the electrostatic interactions of urea and carboxylic groups at the Zn^{2+} active site, there are also lipophilic interactions with an accessible hydrophobic pocket adjacent to the S1 subpocket.[39,41] In general, mechanistic explanations of dissimilarities in inhibition constants for putative PSMA inhibitors highlight the importance of the combination of P1 carboxylates, P1 linker length, and the properties of the P1 distal segment. Differences in linker or distal groups lead to different inhibition potencies. Hydrophobic distal functionalities and relatively short linkers engage non-polar residues in the entrance funnel leading to higher affinities.[40,41] The recently discovered arene-binding site (ABS) belongs to a part of the entrance lid of PSMA preferring aryl functionalities, which significantly increases the binding affinity of the respective PSMA inhibitor and thus can be exploited for structure-aided inhibitor design.[54]

PSMA-targeting Glu-NH-CO-NH-Lys(Ahx)-HBED-CC (PSMA-11[55]) has become one of the most successful radiotracers with respect to clinical application over the last few years[56] and has served as the benchmark for our development of modified glutamate–urea inhibitors. Due to the fact that the chelator HBED-CC is not suitable for the stable complexation of relevant therapeutic radionuclides, we now redesigned the linker in order to match the capability of

HBED-CC to bind to the aforementioned PSMA exo-sites, putatively including the hydrophobic pocket of the PSMA S1 site. It has been reported that replacement of the HBED-CC chelator in **29** (PSMA-11) simply by the DOTA chelator, introduced as carboxamide into the molecule, resulted in significant decrease in the tumor-targeting properties in the new compound.[57] In regard to this observation, the favorable tumor-targeting as well as pharmacokinetic properties of prospective DOTA-based compounds can be achieved by corresponding linker alteration.

We, therefore, constructed low-molecular weight PSMA inhibitors by varying systematically the structure of the linker. The different modifications were divided into four sets each based on the chemical similarities in the structural changes of the linker. The first set of compounds included different numbers and arrangement of aromatic rings in the linker area. These compounds, i.e. **11** to **16**, clearly indicate the requirement of aromatic moieties between the pharmacophore and the DOTA chelator. The optimal number of benzene rings is indicated by **14** with three aromatic moieties in the linker and this compound served as an initial template for further optimizations. As a consequence, the compounds of the second set, i.e. **17** to **20**, including the lead candidate **17** were synthesized. Compound **17**, which contains 2-naphthyl-L-alanine as the first building block of the linker, proved that at least one aromatic moiety with a rigid conformation in the linker seems to be requisite. However, slight changes within the linker building blocks, cf. **18** with 2-naphthyl-D-alanine and **19** with 1-naphthyl-L-alanine, can result in significant alteration of the *in vitro* properties of the PSMA inhibitors. Despite, **20** demonstrated indeed high tumor uptake which, however, was counteracted by high putative background activity. Moreover, the washout of the radioactivity from the kidneys was significantly slower compared to **17**. The preference for 2-naphthyl-L-alanine (**17**) compared to 1-naphthyl-L-alanine (**19**) originates from the perpendicular positioning of the ring system of the 1-naphthyl residue. This formation causes the

steric clash within the PSMA binding pocket which influences the overall binding affinity of the prospective compound. Moreover, the simple sequence interchange of the preferred building blocks 2-naphthyl-L-alanine and *trans*-(aminomethyl)cyclohexanecarboxylic acid in **20** also resulted in a strong deterioration of the compound's desired pharmacological properties.

The third set of DOTA-conjugated PSMA inhibitors, i.e. **21** to **24**, evaluates the influence of the building block while maintaining the 2-naphthyl-L-alanine building block as a constant in the linker. The results provide evidence that 2-naphthyl-L-alanine alone cannot afford favorable properties as, e.g., **21** showed significantly reduced binding affinity ($p = 0.0276$) and internalization ($p = 0.0040$). In general, an additional aromatic moiety, e.g., **22**, improves the characteristics of the inhibitor compared to the insertion of acyclic, non-aromatic building blocks, as shown by **23** with an aminohexanoic acid linker. However, **22** demonstrated significantly lower washout of the radioactivity from the kidneys compared to **17**, most probably due to its higher lipophilicity.

The last set of compounds, i.e. **25** to **28**, examines the importance of the cyclohexane moiety in the linker and proves again the need for additional aromatic moieties between the pharmacophore and the DOTA chelator. Without any aromatic moieties, significant reduction of both PSMA inhibition potency and internalization into LNCaP cells was observed. Thus, aromatic moieties can be considered as crucial for efficient tumor targeting of PSMA inhibitors. This assertion was amply demonstrated by compounds **25**, **26**, and **27**. Additionally, the μPET imaging for **27** revealed high background activity, especially in the lungs and brain, which refers to the aggregation of the compound *in vivo*. With the insertion of a benzene moiety, e.g. (aminomethyl)benzoic acid, in addition to a cyclohexane moiety, the internalization at least is regained in this set of compounds (**28**). This compound demonstrated also high tumor uptake,

however, the clearance from the tumor as well as other organs (e.g. kidneys) was very fast within a short time period.

In general, we observed significant differences between individual compounds which are dependent on the nature of the linkers. Especially the PSMA inhibition potency, the cellular internalization, and also the *in vivo* imaging quality, can be beneficially influenced by careful selection of the linker moiety. Coronal scans obtained from dynamic PET measurements showed differential tumor uptake, background activity, and clearance from the kidneys. Moreover, there are no significant interactions of the PSMA inhibitors with serum proteins which may affect disadvantageously their biodistribution and rate of excretion from the body. Significantly, the *in vitro* results, especially the internalization of the ligands in LNCaP cells, correlate highly with the *in vivo* tumor imaging properties. Thus, cellular internalization *in vitro* seems to be an important indicator of successful tumor uptake.

The aqueous solubility of small molecules depends on their hydrophobicity. Introduced hydrophobic group(s) in the linker may interfere with the PSMA target-inhibitor interaction as the determined log*D* values of these PSMA inhibitors clearly show that the lipophilicity influences both clearance by the kidneys and the background activity. In order to select the most promising compound, SUV_{mean} values in LNCaP tumor, muscle (representing background activity), and kidneys were compared by analysis of the μPET scans. The best combination of all desirable properties was possessed by **17**. While compounds **14**, **16**, and **18** showed similar, or even higher, tumor uptake than **17**, they also exhibited higher background activity as well as increased kidney uptake. Thus, **17** displayed the highest T-to-B ratio (8.5) 1 hour post-injection.

Its fast renal clearance of radioactivity is important to reduce potential radiation toxicity to the kidneys as a possible chronic long-term side effect of PSMA-specific endoradiotherapy.

By modifying the linker between the pharmacophore and the DOTA chelator, a series of 18 new glutamate–urea-based PSMA inhibitors (**11** to **28**) were synthesized. The pharmacokinetic properties, including PSMA inhibition potencies, cellular internalization, and biodistribution behavior of the DOTA-conjugates can be significantly influenced by modification of the linker. Thus, the chemical constitution of the linker moiety has a significant impact on the *in vivo* tumor-targeting and pharmacokinetic properties of PSMA-targeting radioligands. The approach presented here could potentially lead to a more accurate rational and structure-aided design of new PSMA-targeting radioligands based on the glutamate–urea motif. The ultimate aim is the introduction of the best of these DOTA-conjugated PSMA inhibitors, viz. **17**, as a theranostic radioligand, i.e. a molecular vector which is applicable to both diagnostics and the endoradiotherapy of patients suffering from prostate cancer.

EXPERIMENTAL SECTION

Chemicals. For synthesis and analysis, all chemicals (>95% purity; for radiolabeling, highly pure chemicals) and solvents (HPLC-grade purity; for radiolabeling, metal-free ultra-pure water) were purchased commercially from CheMatech (Dijon, France), Iris Biotech (Marktredwitz, Germany), Merck (Darmstadt, Germany), Sigma–Aldrich (Taufkirchen, Germany), and VWR International (Bruchsal, Germany) and used as received without any further purification or drying.

General Synthesis Outline. The solid-phase synthesis of the peptidomimetic glutamate–urea–lysine binding motif is summarized in Scheme 1. The ensuing coupling of the linker was performed according to standard fluorenylmethoxycarbonyl (Fmoc) protocol (Scheme 2). Finally, conjugation of the DOTA chelator (Scheme 2) was realized using HBTU-activated DOTA-tris(*t*-Bu)ester or DOTA-NHS ester.[57,58]

2-Chloro-tritylresin (0.3 mmol, substitution capacity 1.22 mmol/g, 100–200 MESH) was first agitated in dry dichloromethane (DCM) for 45 min and then washed with dry DCM followed by reaction with 1.2 equiv of Alloc (*ε*-allyloxycarbonyl), Fmoc protected L-lysine [Fmoc-Lys(Alloc)-OH, **1**], and 4.8 equiv of *N*-ethyldiisopropylamine (DIPEA) in 3 mL of dry DCM. The coupling of the first protected amino acid on the resin proceeded over the course of 16 h with gentle agitation.

The lysine-immobilized resin **2** was then washed with DCM with unreacted chlorotrityl groups remaining in the resin blocked with a mixture of DCM, methanol (MeOH), and DIPEA in a ratio of 17:2:1, respectively. Selective removal of the Fmoc-protecting group was realized by washing

with a mixture of dimethylformamide (DMF) and piperidine in a ratio of 1:1 once for 2 min and then once again for 5 min in order to get product **3**.

In the next step, 10 equiv of bis(*t*-Bu)-L-glutamate hydrochloride [H-Glu(O*t*-Bu)-O*t*-Bu·HCl, **i**] were used for generation of the isocyanate of the glutamyl moiety **ii**. An appropriate amount of *t*-Bu-protected glutamate was dissolved in 200 mL of dry DCM followed by, shortly afterwards, the addition of 3 mL of DIPEA. This solution was added dropwise over 4 h to a flask with 1 mmol of ice-cooled bis(trichloromethyl)carbonate (Caution: BTC, also named triphosgene, is toxic and fatal if inhaled) in 5 mL of dry DCM. The lysine-immobilized resin **3** was added afterwards in one portion to the solution of the isocyanate of the glutamyl moiety and stirred for 16 h.

The product **4** was filtered off and washed with DCM. The cleavage of the Alloc-protecting group was realized by reaction with 0.3 equiv of tetrakis-(triphenyl)palladium (TPP palladium) in the presence of 30 equiv of morpholine in dry DCM for 2 h. The reaction was performed in the dark using aluminum foil. To remove residuals of the palladium catalysator, the resin was washed with 1% DIPEA in DMF and subsequently with a solution of sodium diethyldithiocarbamate trihydrate (15 mg/mL) in DMF (10 times for 5 min). The resin-immobilized and *t*-Bu-protected binding motif **5** was dried under vacuum and split into three portions.

Relative to the resin (0.1 mmol), 4 equiv of the first Fmoc-protected building block were activated with 3.92 equiv of HBTU (*O*-(benzotriazol-1-yl)-*N*,*N*,*N*',*N*'-tetramethyluronium hexafluorophosphate) in the presence of 4 equiv of DIPEA in dry DMF. Two min after the addition of DIPEA, the solution was added to the DMF pre-swollen immobilized pharmacophore

5 and agitated for 1 h. Selective removal of the Fmoc-protecting group from the product **6** was realized by washing with a mixture of DMF and piperidine in a ratio of 1:1 once for 2 min and then once again for 5 min in order to obtain the product **7**. Depending on an individual compound, 4 equiv of a second, third, and finally fourth Fmoc-protected building block was reacted with 3.92 equiv of HBTU and 4 equiv of DIPEA in dry DMF followed by the deprotection of the Fmoc-protecting group as per above.

The conjugation of the chelator to the immobilized amino-function of the linker in **7** was performed by either of two different methods. The first strategy used 3.95 equiv HBTU-activated 4 equiv of DOTA-tris(*t*-Bu)ester (2-(4,7,10-tris(2-(*t*-butoxy)-2-oxoethyl)-1,4,7,10-tetraazacyclododecan-1-yl)acetic acid) and 4 equiv of DIPEA in DMF in order to obtain product **8**. The final product, i.e. the series of 18 PSMA inhibitors **11–28**, was obtained by agitation and subsequent cleavage from the resin within 2 h with a mixture consisting of trifluoroacetic acid (TFA), triisopropylsilane, and water in a ratio of 95:2.5:2.5, respectively. The second strategy involved preferential cleavage of the *t*-Bu-protected **7** from the resin using 30% 1,1,1,3,3,3-hexafluoroisopropanol (HFIP) in DCM. After reversed-phase high-performance liquid chromatography (RP-HPLC) purification of the product **9**, 1.5 equiv of DOTA-NHS ester (2,2',2''-(10-(2-((2,5-dioxopyrrolidin-1-yl)oxy)-2-oxoethyl)-1,4,7,10-tetraazacyclododecane-1,4,7-triyl)triacetic acid) and 1.5 equiv of *N*,*N*,*N*-triethylamine (TEA) were added and reacted for 16 h in dry DMF. The mixture of solvents from the product was evaporated and the crude compound was dissolved in acetonitrile (ACN) and water in a ratio of 1:1 for subsequent HPLC purification. After HPLC purification, the remaining *t*-Bu groups in compound **10** were cleaved within 2 h using TFA at room temperature. TFA was evaporated and the crude compound **11–28**

was dissolved in acetonitrile (ACN) and water in a ratio of 1:1 followed with subsequent lyophilization.

General Analytical and Purification Methods. All synthesized compounds (Figure 2) were first purified by RP-HPLC and then analyzed by matrix-assisted laser desorption ionization mass spectrometry (MALDI-MS), 1D ^{1}H and ^{13}C nuclear magnetic resonance (NMR), and 2D NMR techniques, viz. correlation spectroscopy (COSY), heteronuclear single quantum correlation (HSQC), and heteronuclear multiple bond correlation (HMBC).

Both analytical (100 × 4.6 mm) and semi-preparative (100 × 10.0 mm) RP-HPLC columns utilized Chromolith RP-18e stationary phase (Merck, Darmstadt, Germany) with mobile phases consisting of 0.1% TFA in water (A) and 0.1% TFA in ACN (B). For analytical runs, a linear gradient of solvent A (100–0% in 6 min) in solvent B at a flow rate of 4 mL/min was used. For semi-preparative runs, a suitable gradient was determined individually for each compound. All compounds were obtained in >98% purity as determined by HPLC and NMR.

MALDI-MS was performed on a Daltonics Microflex system (Bruker Daltonics, Bremen, Germany). Compounds were mixed with either sinapinic, gentisic, or α-cyano-4-hydroxycinnamic acid (CCA) and applied to a MALDI target. MS were acquired over the range 400–2000 Da with pseudomolecular $[M + H]^+$, $[M + Na]^+$, or $[M + K]^+$ ions detected.

NMR (nuclear magnetic resonance) spectra were acquired using a Bruker Avance II NMR spectrometer equipped with a 5-mm inverse-configuration probe with triple-axis-gradient capability at a field strength of 14.1 T operating at 600.1 and 150.9 MHz for ^{1}H and ^{13}C nuclei, respectively. Spectra were also acquired using a Bruker Avance III NMR spectrometer equipped with a 5-mm, normal-configuration probe with z-axis gradient capability at a field strength of 9.4

T operating at 400.1 and 100.6 MHz for ^{1}H and ^{13}C nuclei, respectively, using the lower field to combat dynamic effects. Spectra were acquired at 30, 70, or 90 °C where indicated to further combat dynamic effects with samples contained in d_6-DMSO. Pulse widths were calibrated following the described protocol.[59] The chemical shifts of ^{1}H and ^{13}C nuclei are reported relative to TMS (δ = 0 ppm for both ^{1}H and ^{13}C) using the solvent signals as secondary internal references (δ = 2.50 ppm for ^{1}H and δ = 39.52 ppm for ^{13}C). The chemical shifts of ^{1}H nuclei are reported to three decimal places when the spin system was amenable to first-order analysis or to two decimal places when the multiplet was beyond such interpretation, the overlap of signals precluded such, or chemical shifts were taken from 2D NMR spectra–particularly in the case of signals obscured by the water signal. The signal intensity of ^{1}H NMR signals were set to the nearest integer value of measured integral values; for overlapped signals and signals obscured by the water signal, intensity was apportioned according to HSQC/DEPT results. The chemical shifts of ^{13}C nuclei are reported to two decimal places when sharp signals were observable directly or one decimal place when the peak was broad or the signal was observed indirectly. General NMR experimental and acquisition details for 1D ^{1}H, ^{13}C, and DEPT observation and standard gradient-selected 2D COSY, HSQC, and HMBC spectra and routine chemical shift assignment using 2D NMR have been previously described.[60–63] UDEFT[64,65] spectra were acquired and processed as described[64] with Acq and PAD times of 0.2 and 4 s, respectively, and with linear prediction of the FIDs; otherwise parameters were the same as normal ^{13}C acquisition. Partial and tentative assignments of compounds, for which 1D NMR spectra (single-pulse acquisition for ^{1}H and ^{13}C nuclei and DEPT acquisition for ^{13}C nuclei) only were acquired, were accomplished by comparative analysis to fully assigned structures (**12**, **14**, **17**, and **19**) and

by iterative calculation of chemical shifts using the chemical shift prediction routine within the ChemDraw 12.0 program.

Radiolabeling. Positron-emitting ^{68}Ga [$E_{\beta+,max}$ = 1.9 MeV (88%)] was eluated from a ^{68}Ge ($t_{½}$ = 271 d)/^{68}Ga ($t_{½}$ = 68 min)[66] generator based on pyrogallol resin support[67] as [^{68}Ga]$GaCl_3$ in 0.1 M HCl. The radioisotope ^{177}Lu ($t_{½}$ = 6.71 days) β^--emitting radionuclide [$E_{\beta^-,max}$ = 497 keV (79%)] with few γ-emissions [$E_{\gamma/x}$ = 113 keV (6%), 208 keV (11%)][66] was purchased from PerkinElmer (Rodgau, Germany) as [^{177}Lu]$LuCl_3$ in 0.05 M HCl.

Radiolabeling with ^{68}Ga was accomplished using 30 μL of [^{68}Ga]Ga^{3+} eluate (~100 MBq) with 70 μL of 2.4 M HEPES (4-(2-hydroxyethyl)-1-piperazineethanesulfonic acid, pH 7.5). This solution was adjusted with 10 or 30% NaOH to pH 4.2. Subsequently, 0.5–1 nmol of compound diluted in 0.1 M HEPES was added and the reaction mixture was heated at 95–98 °C for 15 min. The labeling efficiency was determined by RP-HPLC as per above or by RP-TLC (RP-thin-layer chromatography) over silica gel plates (60 RP-18 F_{254S}) using 0.1 M sodium citrate as the mobile phase. ^{68}Ga-labeling resulted in a labeling efficiency >95% for all tested PSMA-inhibitors. The specific activities for ^{68}Ga-labeled compounds were in the range of 100–200 GBq/μmol.

^{177}Lu-Labeling was performed with 5 μL of [^{177}Lu]$LuCl_3$ (~25 MBq), 112 μL of 0.4 M sodium acetate (pH 5.0), and 0.5–1 nmol of compound in 0.1 M HEPES at 95 °C for 20 min. The specific activities for ^{177}Lu-labeled compounds were in the range of 25–50 GBq/μmol and the labeling efficiency was >98% for all compounds.

Assays. For *in vivo* assays, radiolabeled compounds were additionally purified via Sep-Pak C18 Plus Light cartridges (Waters, Milford, USA). After dilution with 500 μL of phosphate buffered saline (PBS), the reaction mixture was applied directly to and trapped on a preconditioned Sep-

Pak cartridge equilibrated with PBS. The cartridge was subsequently flushed with 1 mL of PBS followed by 10 mL of air. The pure compound was then eluted with 70% ethanol and evaporated to dryness. The radiochemical yield (RCY) for all labeled compounds then exceeded >99%.

The potential binding to the serum proteins was performed with seven representative compounds, viz. **11**, **14**, **17**, **22**, **26**, and **28**, and analyzed on a Superdex^{TM} 75 5/150 GL column (GE Healthcare, Munich, Germany) after 1 h incubation at 37 °C. The mobile phase consisted of PBS (pH 7.4) and the runs were performed at a flow rate of 0.4 mL/min. The lipophilicities of all compounds were determined by their equilibrium distribution after thorough shaking in a two-phase system consisting of *n*-octanol and 0.1 M HEPES (pH 7.4). Small aliquots from both phases were collected and analyzed in a gamma counter in order to calculate distribution coefficients (log*D*, Equation 1).

In vitro experiments were performed using the PSMA$^+$ LNCaP cell line (European Collection of Cell Cultures, Salisbury, UK) derived from an androgen-sensitive human lymph node metastatic lesion of prostatic adenocarcinoma (ATCC CRL-1740). The cells were grown in RPMI 1640 medium (PAN-Biotech, Aidenbach, Germany) supplemented with 10% fetal calf serum (FCS) and 1% L-glutamine. Cell cultures were maintained in an atmosphere of 5% CO_2 at 37 °C in a humidified incubator. For *in vivo* experiments (μPET imaging), six- to eight-week-old male BALB/c nu/nu mice (The Jackson Laboratory, Maine, USA) were implanted subcutaneously in the right trunk with LNCaP cells (6×10^6) in 100 μL of 50% Matrigel (Discovery Labware, Inc., Bedford, MA, USA) in Opti-MEM (Life Technologies GmbH, Darmstadt, Germany). Mice were imaged when the tumor xenografts reached approximately 1 cm in diameter whereupon the radiolabeled compound was injected via the tail vein (~30 MBq, 0.5 nmol, specific activity ~60 GBq/μmol).

The binding affinity was determined using a cell-based competitive assay with ^{68}Ga-labeled [Glu-NH-CO-NH-Lys(Ahx)]$_2$-HBED-CC (PSMA-10[58]) and expressed as K_i values. Compounds at twelve different concentrations (0, 0.5, 1, 2.5, 5, 10, 25, 50, 100, 500, 1000 and 5000 nM) were incubated with 0.75 nM of ^{68}Ga-**30** (PSMA-10) together with LNCaP cells (10^5 LNCaP cells/well). After 45 min incubation at 37 °C, the cells were washed three times with of ice-cold PBS. Radioactivity accumulated in the cells was measured by a gamma counter and the data fitted using a nonlinear regression algorithm (GraphPad Software) to calculate 50% inhibitory concentrations (IC_{50} values).

For the determination of internalization, LNCaP cells (10^5 LNCaP cells/well) were seeded in poly-L-lysine coated plates 24 h before the experiment. The cells were incubated for 45 min at 37 °C with 32 nM of ^{177}Lu-labeled compound (25 GBq/μmol) in 250 μL Opti-MEM. Additionally, for confirmation of specific cellular uptake, the second set of compounds was also treated with 500 μM/well of PSMA-inhibitor 2-PMPA (2-(phosphonomethyl)pentane-1,5-dioic acid). The cells were washed four times with ice-cold PBS and the surface-bound radioactivity was removed by washing twice with 50 mM glycine (pH 2.8). After washing the cells with PBS, the internalized fraction was determined by lysis of the LNCaP cells using 0.3 M NaOH. The radioactivity collected from the glycine and hydroxide fractions was measured in a gamma counter and calculated as %IA/10^6 LNCaP cells. Additionally, the specific cell surface binding and specific internalization were calculated by subtracting the non-specific cell surface binding and the non-specific internalized fraction and expressed again as %IA/10^6 LNCaP cells.

Anaesthetized mice (2% sevoflurane, Abbott) were injected with ^{68}Ga-labeled compound and placed in a small animal PET scanner (Inveon PET, Siemens). Each examination was performed

up to 2 h post-injection and included a 15 min transmission scan before the injection of ^{68}Ga-labeled compound, a 60 min emission scan, a second transmission scan, and a final emission scan 100 to 120 min post-injection. For testing each compound, one exemplary animal was used.

In vitro experiments (inhibition potency, surface-binding, and internalization) were performed in triplicate. Calculated IC_{50} values were converted into K_i values by the Cheng–Prusoff method[68] (Equation 2) which express the inhibition potency of the respective compound, using the experimentally determined K_d value of ^{68}Ga-**30** (3.8 ± 1.8 nM). Data were expressed as means ± SD (standard deviation for confidence interval) where p values <0.05 were considered statistically significant. p Values were calculated as unpaired two-sided *t*-test assuming the gaussian distribution. Scans from μPET imaging were reconstructed iteratively using the space alternating generalized expectation maximization method (SAGE, 16 subsets, 4 iterations) applying median root prior correction and were converted to standardized uptake value (SUV) images. Quantitation was accomplished using an ROI technique and expressed as SUVmean.

ANCILLARY INFORMATION

Supporting Information

NMR data and spectra for all synthesized DOTA-conjugated PSMA-inhibitors. This material is available free of charge via the Internet at http://pubs.acs.org.

Corresponding Author

*M.E.: phone/fax, +49 6221 56 7127; E-mail, m.eder@dkfz-heidelberg.de.

Author Contributions

$^{\perp}$ K.K. and M.E. contributed equally to this work and share senior authorship.

Notes

The authors declare no competing financial interest.

Acknowledgements

Financial support for a Helmholtz International Graduate School for Cancer Research Ph.D stipend for M.B., a DFG grant for M.E. (ED234/2-1), and a Klaus Tschira Foundation grant for U.H. are all gratefully acknowledged. All animal experiments complied with the current laws of the Federal Republic of Germany and were conducted according to German Animal Welfare guidelines. Biodistribution and μPET imaging studies were kindly performed by Ursula Schierbaum and Karin Leotta from the German Cancer Research Center, Heidelberg, Germany. The authors would like to also thank to Lukas Welti for the initial realization of the topic.

Abbreviations used

PSMA, prostate-specific membrane antigen; HPLC, high-performance liquid chromatography; TLC, thin-layer chromatography; Glu, glutamate; Lys, lysine; TFA, trifluoroacetic acid; DOTA, 1,4,7,10-tetraazacyclododecane-1,4,7,10-tetraacetic acid; HBED-CC, *N,N′*-bis-[2-hydroxy-5-(carboxyethyl)benzyl]ethylenediamine-*N,N′*-diacetic acid; 2D, two dimensional; 1D, one dimensional; μ, micro; °C, degrees Celsius; aa, amino acid; FDG, 2-fluoro-2-deoxy-D-glucose; Ala, alanine; COSY, correlation spectroscopy; DCM, dichloromethane; DMSO, dimethylsulfoxide; Fmoc, 9-fluorenylmethylmethoxycarbonyl; FT, Fourier transform; HSQC, heteronuclear single quantum correlation; HMBC, heteronuclear multiple bond correlation; UDEFT, uniform driven equilibrium Fourier transform; IC_{50}, half-maximum inhibitory concentration; *J*, coupling constant; K_i, inhibition constant; log*D*, logarithm of distribution coefficient; *m*/*z*, mass-to-charge ratio; MALDI-MS, matrix-assisted laser desorption ionization mass spectrometry; NMR, nuclear magnetic resonance; R_f, retention factor; rt; room temperature; *t*-Bu, *tert*-butyl; PET, positron emission tomography; SPECT, single photon emission computed tomography; SUV, standardized uptake value; DMF, dimethylformamide; MIP, maximum intensity projections; SAR, structure–activity relationships; RCY, radiochemical yield; AMBA, 4-(Fmoc-aminomethyl)benzoic acid; Ahx, 6-(Fmoc-amino)hexanoic acid; AMCH, *trans*-4-(Fmoc-aminomethyl)cyclohexanecarboxylic acid; br, broad; d, doublet; ho, higher order; m, multiplet; ol, overlapped; t, triplet; qt, quartet; s, singlet; v, very.

REFERENCES

(1) Siegel, R.; Ma, J.; Zou, Z.; Jemal, A. Cancer statistics, 2014. *CA-Cancer J. Clin.* **2014**, *64*, 9–29.

(2) Ferlay, J.; Steliarova-Foucher, E.; Lortet-Tieulent, J.; Rosso, S.; Coebergh, J. W. W.; Comber, H.; Forman, D.; Bray, F. Cancer incidence and mortality patterns in Europe: Estimates for 40 countries in 2012. *Eur. J. Cancer* **2013**, *49*, 1374–1403.

(3) Schröder, F. H.; Hugosson, J.; Roobol, M. J.; Tammela T. L. J.; Zappa, M.; Nelen, V.; Kwiatkowski, M.; Lujan, M.; Määttänen, L.; Lilja, H.; Denis, L. J.; Recker, F.; Paez, A.; Bangma, C. H.; Carlsson, S.; Puliti, D.; Villers, A.; Rebillard, X.; Hakama, M.; Stenman, U. H.; Kujala, P.; Kimmo, T.; Aus, G. Screening and prostate cancer mortality: results of the European Randomised Study of Screening for Prostate Cancer (ERSPC) at 13 years of follow-up. *Lancet* **2014**, *384*, 2027–2035.

(4) Edwards, B. K.; Noone, A. M.; Mariotto, A. B.; Simard, E. P.; Boscoe, F. P.; Henley, S. J.; Jemal A.; Cho, H.; Anderson, R. N.; Kohler, B. A.; Eheman, C. R.; Ward, E. M. Annual Report to the Nation on the status of cancer, 1975–2010, featuring prevalence of comorbidity and impact on survival among persons with lung, colorectal, breast, or prostate cancer. *Cancer* **2014**, *120*, 1290–1314.

(5) Thompson, I. M.; Tangen, C. M. Prostate cancer screening comes of age. *Lancet* **2014**, *384*, 2004–2006.

(6) Kim M. M.; Hoffman, K. E.; Levy, L. B.; Frank, S. J.; Pugh, T. J.; Choi, S.; Nguyen, Q. N.; McGuire, S. E.; Lee, A. K.; Kuban, D. A. Improvement in prostate cancer survival over time: A 20-year analysis. *Cancer J*. **2012**, *18*, 1–8.

(7) Silver, D. A.; Pellicer, I.; Fair W. R.; Heston, W. D.; Cordon-Cardo, C. Prostate-specific membrane antigen expression in normal and malignant human tissues. *Clin. Cancer Res*. **1997**, *3*, 81–85.

(8) Kularatne, S. A.; Wang, K.; Santhapuram, H. K.; Low, P. S. Prostate-specific membrane antigen targeted imaging and therapy of prostate cancer using a PSMA inhibitor as a homing ligand. *Mol. Pharm*. **2009**, *6*, 780–789.

(9) Dumas, F.; Gala, J. L.; Berteau, P.; Brasseur, F.; Eschwége, P.; Paradis, V.; Lacour, B.; Philippe, M.; Loric, S. Molecular expression of PSMA mRNA and protein in primary renal tumors. *Int. J. Cancer* **1999**, *80*, 799–803.

(10) Gala, J. L.; Loric, S.; Guiot, Y.; Denmeade, S. R.; Gady, A.; Brasseur, F.; Heusterspreute, M.; Eschwege, P.; De Nayer, P.; Van Cangh, P.; Tombal, *B*. Expression of prostate-specific membrane antigen in transitional cell carcinoma of the bladder: prognostic value? *Clin. Cancer Res*. **2000**, *6*, 4049–4054.

(11) Chang, S. S.; Reuter, V. E.; Heston, W. D.; Bander, N. H.; Grauer, L. S.; Gaudin, P. B. Five different anti-prostate-specific membrane antigen (PSMA) antibodies confirm PSMA expression in tumor-associated neovasculature. *Cancer Res*. **1999**, *59*, 3192–3198.

(12) Haffner, M. C.; Kronberger, I. E.; Ross, J. S.; Sheehan, C. E.; Zitt, M.; Mühlmann, G.; Ofner, D.; Zelger, B.; Ensinger, C.; Yang, X. J.; Geley, S.; Margreiter, R.; Bander, N. H.

Prostate-specific membrane antigen expression in the nevasculature of gastric and colorectal cancers. *Hum. Pathol*. **2009**, *40*, 1754–1761.

(13) Eder, M.; Eisenhut, M.; Babich, J.; Haberkorn, U. PSMA as a target for radiolabelled small molecules. *Eur. J. Nucl. Med. Mol. Imaging* **2013**, *40*, 819–823.

(14) Maresca, K. P.; Hillier, S. M.; Lu, G.; Marquis, J. C.; Zimmerman, C. N.; Eckelman, W. C.; Joyal, J. L.; Babich, J. W. Small molecule inhibitors of PSMA incorporating technetium-99m for imaging prostate cancer: Effects of chelate design on pharmacokinetics. *Inorg. Chim. Acta* **2012**, *389*, 168–175.

(15) Banerjee, S. R.; Foss, C. A.; Castanares, M.; Mease, R. C.; Byun, Y.; Fox, J. J.; Hilton, J.; Shawn, E.; Lupold, A.; Kozikowski, P.; Pomper, M. G. Synthesis and evaluation of technetium-99m- and rhenium-labeled inhibitors of the prostate-specific membrane antigen (PSMA). *J. Med. Chem.* **2008**, *51*, 4504–4517.

(16) Lesche, R.; Kettschau, G.; Gromov, A. V.; Böhnke, N.; Borkowski, S.; Mönning, U.; Hegele-Hartung, U.; Döhr, O.; Dinkelborg, L. M.; Graham, K. Preclinical evaluation of BAY 1075553, a novel ^{18}F-labelled inhibitor of prostate-specific membrane antigen for PET imaging of prostate cancer. *Eur. J. Nucl. Med. Mol. Imaging* **2014**, *41*, 89–101.

(17) Tykvart, J.; Navrátil, V.; Sedlák, F.; Corey, E.; Colombatti, M.; Fracasso, G.; Koukolík, F.; Bařinka, C.; Šácha, P.; Konvalinka, J. Comparative analysis of monoclonal antibodies against prostate-specific membrane antigen (PSMA). *Prostate* **2014**, *74*, 1674–1690.

(18) Pandit-Taskar, N.; O'Donoghue, O.; Beylergil, V.; Lyashchenko, S.; Ruan, S.; Solomon, S. B.; Durack, J. C.; Carrasquillo, J. A.; Lefkowitz, R. A.; Gonen, M.; Lewis, J. S.; Holland, J.

P.; Cheal, S. M.; Reuter, V. E.; Osborne, J. R.; Loda, M. F.; Smith-Jones, P. M., Weber, W. A.; Bander, N. H.; Scher, H. I.; Morris, M. J.; Larson, S. M. ^{89}Zr J591 immuno-PET imaging in patients with advanced metastatic prostate cancer. *Eur. J. Nucl. Med. Mol. Imaging* **2014**, *41*, 2093–2105.

(19) Behe, M.; Alt, K.; Deininger, F.; Bühler, P.; Wetterauer, U.; Weber, W. A.; Elsässer-Beile, U.; Wolf, P. *In vivo* testing of ^{177}Lu-labelled anti-PSMA antibody as a new radioimmunotherapeutic agent against prostate cancer. *In Vivo* **2011**, *25*, 55–59.

(20) Chu, T. C.; Marks, J. W.; Lavery, L. A.; Faulkner, S.; Rosenblum, M. G.; Ellington, A. D.; Levy, M. Aptamer: toxin conjugates that specifically target prostate tumor cells. *Cancer Res*. **2006**, *66*, 5989–5892.

(21) Wu, X.; Ding, B.; Gao, J.; Wang, H.; Fan, W.; Wang, X.; Zhang, W.; Wang, X.; Ye, L.; Zhang, M.; Ding, X.; Liu, J.; Zhu, Q.; Gao, S. Second-generation aptamer-conjugated PSMA-targeted delivery system for prostate cancer therapy. *Int. J. Nanomed.* **2011**, 6, 1747–1756.

(22) Baek, S. E.; Lee, K. H.; Park, Y. S.; Oh, D. K.; Oh, S.; Kim, K. S.; Kim, D. E. RNA aptamer-conjugated liposome as an efficient anticancer drug delivery vehicle targeting cancer cells *in vivo*. *J. Controlled Release* **2014**, *196*, 234–242.

(23) Kasten, B. B.; Liu, T.; Nedrow-Byers, J. R.; Benny, P. D.; Berkman, C. E. Targeting prostate cancer cells with PSMA inhibitor-guided gold nanoparticles. *Bioorg. Med. Chem. Lett*. **2013**, *23*, 565–568.

(24) Mukherjee, A.; Darlington, T.; Holz, R.; Holz, C.; Olson, S.; Kulkami, P.; DeWeese, T. L.; Getzenberg, R. H.; Ivkov, R.; Lupold, S. E. Development and screening of a series of

antibody-conjugated and silica-coated iron oxide nanoparticles for targeting the prostate-specific membrane antigen. *ChemMedChem* **2014**, *9*, 1356–1360.

(25) Hrkach, J.; Von Hoff, D.; Ali, M. M.; Andrianova, E.; Auer, J.; Campbell, T.; De Witt, D.; Figa, M.; Figueiredo, M.; Horhota, A.; Low, S.: McDonnell, K.; Peeke, E.; Retnarajan, B.; Sabnis, A.; Schnipper, E.; Song, J. J.; Song, Y. H.; Summa, J.; Tompsett, D.; Troiano, G.; Van Geen Hoven, T.; Wright, J.; LoRusso, P.; Kantoff, P. W.; Bander, N. H.; Sweeney, C.; Farokhzad, O. C.; Langer, R.; Zale, S. Preclinical development and clinical translation of a PSMA-targeted docetaxel nanoparticle with a differentiated pharmacological profile. *Sci. Transl. Med*. **2012**, *4*, 128–139.

(26) Taneja, S. S. ProstaScint® scan: contemporary use in clinical practice. *Rev. Urol*. **2004**, *6*, 19–28.

(27) Sodee, D. B.; Malguria, N.; Faulhaber, P.; Resnick, M. I.; Albert, J.; Bakale, G. Multicenter ProstaScint® imaging findings in 2154 patients with prostate cancer. *Urology* **2000**, *56*, 988–993.

(28) Bander, N. H. Technology insight: monoclonal antibody imaging of prostate cancer. *Nat. Clin. Pract. Urol*. **2006**, *3*, 216–225.

(29) Barren, R. J.; Holmes, E. H.; Boynton, A. L.; Misrock, S. L.; Murphy, G. P. Monoclonal antibody 7E11.C5 staining of viable LNCaP cells. *Prostate* **1997**, *30*, 65–68.

(30) Nanus, D. M.; Milowski, M. I.; Kostakoglu, L.; Smith-Jones, P. M.; Vallabahajosula, S.; Goldsmith, S. J.; Bander, N. H. Clinical use of monoclonal antibody HuJ591 therapy: targeting prostate specific membrane antigen. *J. Urol.* **2003**, *170*: S84–S89.

(31) Vallabahajosula, S.; Smith-Jones, P. M.; Navarro, V.; Goldsmith, S. J.; Bander, N. H. Radioimmunotherapy of prostate cancer in human xenografts using monoclonal antibodies specific to prostate specific membrane antigen (PSMA): studies in nude mice. *Prostate* **2004**, *58*, 145–155.

(32) Olafsen, T.; Bartlett, D.; Ho, D.; Zhang, G.; Torgov, M.; Keppler, J.; Behrenbruch, Ch.; Wu, A.; Pandit-Taskar, N.; Morris, M. J.; Lewis, J. S.; Lyashchenko, S. K.; Gudas, J. M. Minibody imaging of prostate-specific membrane antigen (PSMA): From concept to clinic. *J. Clin. Oncol*. **2014**, *32* (suppl; abstr. e16057).

(33) Weineisen, M.; Schottelius, M.; Simecek, J.; Baum, R. P.; Yildiz, A.; Beykan, S.; Kulkarni, H. R.; Lassmann, M.; Klette, I.; Eiber, M.; Schwaiger, M.; Wester, H, J. ^{68}Ga- and ^{177}Lu-labeled PSMA I&T: optimization of a PSMA-targeted theranostic concept and first proof-of-concept human studies. *J. Nucl. Med*. **2015**, *56*, 1169–1176.

(34) Banerjee, S. R.; Pullambhatla, M.; Byun, Y.; Nimmagadda, S.; Green, G.; Fox, J. J.; Horti, A.; Mease, R. C.; Pomper, M. G. ^{68}Ga-labeled inhibitors of prostate-specific membrane antigen (PSMA) for imaging prostate cancer. *J. Med. Chem.* **2010**, *53*, 5333–5341.

(35) Chen, Y.; Foss, C. A.; Byun, Y.; Nimmagadda, S.; Pullambhatla, M.; Fox, J. J.; Castanares, M.; Lupold, S. E.; Babich, J. W.; Mease, R. C.; Pomper, M. G. Radiohalogenated prostate-specific membrane antigen (PSMA)-based ureas as imaging agents for prostate cancer. *J. Med. Chem*. **2008**, *51*, 7933–7943.

(36) Foss, C. A.; Mease, R. C.; Fan, H.; Wang, Y.; Ravert, H. T.; Dannals, R. F.; Olszewski, R. T.; Heston, W. D.; Kozikowski, A. P.; Pomper, M. G. Radiolabeled small-molecule ligands

for prostate-specific membrane antigen: in vivo imaging in experimental models of prostate cancer. *Clin. Cancer Res*. **2005**, *11*, 4022–4028.

(37) Barinka, C.; Rojas, C.; Slusher, B.S.; Pomper, M. Glutamate carboxypeptidase II in diagnosis and treatment of neurologic disorders and prostate cancer. *Curr. Med. Chem.* **2012**, *19*, 856–870.

(38) Anderson, M. O.; Wu, L. Y.; Santiago, N. M.; Moser, J. M.; Rowley, J. A.; Bolstad, E. S. D.; Berkman C. E. Substrate specificity of prostate-specific membrane antigen. *Bioorg. Med. Chem.* **2007**, *15*, 6678–6686.

(39) Mesters, J. R.; Barinka, C.; Li, W.; Tsukamoto, T.; Majer, P.; Slusher, B. S.; Konvalinka, J.; Hilgenfeld, R. Structure of glutamate carboxypeptidase II, a drug target in neuronal damage and prostate cancer. *EMBO J.* **2006**, *25*, 1375–1384.

(40) Barinka, C.; Hlouchová, K.; Rovenská, M.; Majer, P.; Dauter, M.; Hin, N.; Ko, Y. S.; Tsukamoto T.; Slusher, B. S.; Konvalinka, J.; Lubkowski, J. Structural basis of interactions between human glutamate carboxypeptidase II and its substrate analogs. *J. Mol. Biol.* **2008**, *376*, 1438–1450.

(41) Barinka, C.; Byun, Y.; Dusich, C. L.; Banerjee, S. R.; Chen, Y.; Castanares, M.; Kozikowski, A. P.; Mease, R. C.; Pomper, M. G.; Lubkowski, J. Interactions between human glutamate carboxypeptidase II and urea-based inhibitors: structural characterization. *J. Med. Chem*. **2008**, *51*, 7737–7743.

(42) Davis, M. I.; Bennett, M. J.; Thomas, L. M.; Bjorkman, P. J. Crystal structure of prostate-specific membrane antigen, a tumor marker and peptidase. *Proc. Natl. Acad. Sci. U.S.A.* **2005**, *102*, 5981–5986.

(43) Banerjee, R. S.; Pullambhatla, M.; Shallal, H.; Lisok, A.; Mease, R. C.; Pomper, M. G. Modular strategy to prepare multivalent inhibitors of prostate-specific membrane antigen (PSMA). *Oncotarget* **2011**, *2*, 1244–1253.

(44) Benešová, M.; Schäfer, M.; Bauder-Wüst, U.; Afshar-Oromieh, A.; Kratochwil, C.; Mier, W.; Haberkorn, U.; Kopka, K.; Eder, M. Preclinical evaluation of a tailor-made DOTA-conjugated PSMA inhibitor with optimized linker moiety for imaging and endoradiotherapy of prostate cancer. *J. Nucl. Med.* **2015**, *56*, 914–920.

(45) Caroli, P.; Nanni, C.; Rubello, D.; Alavi, A.; Fanti, S. Non-FDG PET in the practice of oncology. *Indian J. Cancer* **2010**, *47*, 120–125.

(46) Hao, G.; Zhou, J.; Guo, Y.; Long, M. A.; Anthony, T.; Stanfield, J.; Hsieh, J. T.; Sun, X. A cell permeable peptide analog as a potential-specific PET imaging probe for prostate cancer detection. *Amino Acids* [Online early access]. DOI: 10.1007/s00726-010-0515-5. Published Online: Mar 10, 2010.

(47) Hain, S. F.; Maisey, M. N. Positron emission tomography in urological tumours. *BJU Int.* **2003**, *92*, 159–64.

(48) Rioja, J.; Rodríguez-Fraile, M.; Lima-Favaretto, R.; Rincón-Mayans, A.; Peñuelas-Sánchez, I.; Zudaire-Bergera, J., J.; Parra, R. O. Role of positron emission tomography in urological oncology. *BJU Int*. **2010**, *106*, 1578–1593.

(49) Reske, S. N. [^{11}C]choline uptake with PET/CT for the initial diagnosis of prostate cancer: relation to PSA levels, tumor stage and anti-androgenic therapy. *Eur. J. Nucl. Med. Mol. Imaging* **2008**, *35*, 1740–1741.

(50) Reske, S. N.; Blumstein, N. M.; Glatting, G. [^{11}C]choline PET/CT imaging in occult local relapse of prostate cancer after radical prostatectomy. *Eur. J. Nucl. Med. Mol. Imaging* **2008**, *35*, 9–17.

(51) Regino, C. A.; Wong, K. J.; Milenic, D. E.; Holmes, E.H.; Garmestani, K.; Choyke, P. L.; Brechbiel, M. W. Preclinical evaluation of a monoclonal antibody (3C6) specific for prostate-specific membrane antigen. *Curr. Radiopharm.* **2009**, *2*, 9–17.

(52) Elsässer-Beile, U.; Wolf, P.; Gierschner. D.; Bühler, P.; Schultze-Seemann, W.; Wetterauer, U. A new generation of monoclonal and recombinant antibodies against cell-adherent prostate specific membrane antigen for diagnostic and therapeutic targeting of prostate cancer. *Prostate* **2006**, *66*, 1359–1370.

(53) Elsässer-Beile, U.; Reischl, G.; Wiehr, S.; Bühler, P.; Wolf, P.; Alt, K.; Shively, J.; Judenhofer, M. S.; Machulla, H. J.; Pichler, B. J. PET imaging of prostate cancer xenografts with a highly specific antibody against the prostate-specific membrane antigen. *J. Nucl. Med.* **2009**, *50*, 606–611.

(54) Zhang, A. X.; Murelli, R. P.; Barinka, C.; Michel, J.; Cocleaza, A.; Jorgensen, W. L.; Lubkowski, J.; Spiegel, D. A. A remote arene-binding site on prostate specific membrane antigen revealed by antibody-recruiting small molecules. *J. Am. Chem. Soc.* **2010**, *132*, 12711–12716.

(55) Eder, M.; Neels, O.; Müller, M.; Bauder-Wüst, U.; Remde, Y.; Schäfer, M.; Hennrich, U.; Eisenhut, M.; Afshar-Oromieh, A.; Haberkorn, U.; Kopka, K. Novel preclinical and radiopharmaceutical aspects of [^{68}Ga]Ga-PSMA-HBED-CC: a new PET tracer for imaging of prostate cancer. *Pharmaceuticals* **2014**, *7*, 779–796.

(56) Afshar-Oromieh, A.; Avtzi, E.; Giesel, F. L.; Holland-Letz, T.; Linhart, H. G.; Eder, M.; Eisenhut, M.; Boxler, S.; Hadaschik, B. A.; Kratochwil, C.; Weichert, W.; Kopka, K.; Debus, J.; Haberkorn, U. The diagnostic value of PET/CT imaging with the ^{68}Ga-labelled PSMA ligand HBED-CC in the diagnosis of recurrent prostate cancer. *Eur. J. Nucl. Med. Mol. Imaging* **2015**, *42*, 197–209.

(57) Eder, M.; Schäfer M.; Bauder-Wüst, U.; Hull, W. E.; Wängler, C.; Mier, W.; Haberkorn, U.; Eisenhut, M. ^{68}Ga-complex lipophilicity and the targeting property of a urea-based PSMA inhibitor for PET imaging. *Bioconjugate Chem.* **2012**, *23*, 688−697.

(58) Schäfer, M; Bauder-Wüst, U.; Leotta, K.; Zoller, F.; Mier, W.; Haberkorn, U.; Eisenhut, M.; Eder, M. A dimerized urea-based inhibitor of the prostate-specific membrane antigen for Ga-68-PET imaging. *Eur. J. Nucl. Med. Mol. Imaging* **2012**, *2*, 23–33.

(59) Klika, K. D. The application of simple and easy to implement decoupling pulse scheme combinations to attain artifact-free reduced decoupling for large *J* values. *Int. J. Spectrosc.* **2014**, Article ID 289638.

(60) Mäki, J.; Tähtinen, P.; Kronberg, L.; Klika, K. D. Restricted rotation/tautomeric equilibrium and determination of the site and extent of protonation in bi-imidazole nucleosides by multinuclear NMR and GIAO-DFT calculations. *J. Phys. Org. Chem.* **2005**, *18*, 240–249.

(61) Virta, P.; Koch, A.; Roslund, M. U.; Mattjus, P.; Kleinpeter, E.; Kronberg, L.; Sjöholm, R.; Klika, K. D. Synthesis, characterisation and theoretical calculations of 2,6-diaminopurine etheno derivatives. *Org. Biomol. Chem.* **2005**, *3*, 2924–2929.

(62) Klika, K. D.; Bernát, J.; Imrich, J.; Chomča, I.; Sillanpää, R.; Pihlaja, K. Unexpected formation of a spiro acridine and fused ring system from the reaction between an *N*-acridinylmethyl substituted thiourea and bromoacetonitrile under basic conditions. *J. Org. Chem.* **2001**, *66*, 4416–4418.

(63) Balentová, E.; Imrich, J.; Bernát, J.; Suchá, L.; Vilková, M.; Prónayová, N.; Kristian, P.; Pihlaja, K.; Klika, K. D. Stereochemistry, tautomerism, and reactions of acridinyl thiosemicarbazides in the synthesis of 1,3-thiazolidines. *J. Heterocycl. Chem.* **2006**, *43*, 645–656.

(64) Piotto, M.; Bourdonneau, M.; Elbayad, K.; Wieruszeski, J.-M.; Lippens, G. New DEFT sequences for the acquisition of one-dimensional carbon NMR spectra of small unlabelled molecules. *Magn. Reson. Chem.* **2006**, *44*, 943–947.

(65) Becker, E. D.; Ferretti, J. A.; Farrar, T. C. Driven Equilibrium Fourier Transform Spectroscopy. A New Method for Nuclear Magnetic Resonance Signal Enhancement. *J. Am. Chem. Soc.* **1969**, *91*, 7784–7785.

(66) Firestone, R. B.; Shirley, V. S.; Baglin, C. M.; Chu, S. Y. F.; Zipkin, J. *Table of Isotopes*, Volume I, 8th ed.; John Wiley & Sons, Inc.: New York, **1996**; pp 330, 323–325.

(67) Schuhmacher, J.; Maier-Borst, W. A new Ge-68/Ga-68 radioisotope generator system for production of Ga-68 in dilute HCl. *Int. J. Appl. Radiat. Isot.* **1981**, *32*, 31–36.

(68) Yung-Chi, C.; Prusoff, W. H. Relationship between the inhibition constant (*KI*) and the concentration of inhibitor which causes 50 per cent inhibition (I_{50}) of an enzymatic reaction. *Biochem. Pharmacol. (Amsterdam, Neth.)* **1973**, *22*, 3099–3108.

ARTWORK AND TABLES

FIGURES

Figure 1. General Structure of the PSMA Inhibitors (**11**–**28**) and Compound **29**.

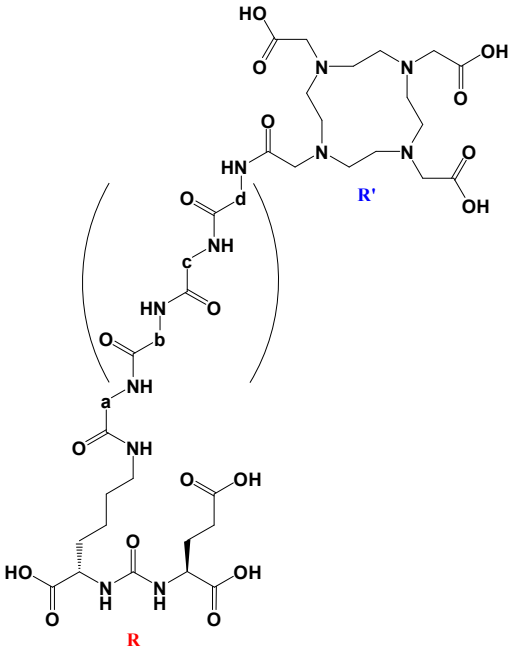

General structure of the PSMA inhibitors

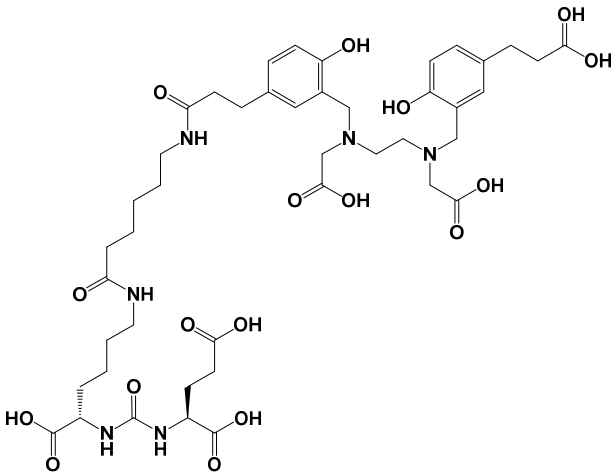

Structure of compound **29** (PSMA-11)

Figure 2. Designation of Prepared Compounds Used in the Text and Their Division into the Four Groups Based on the Structure-similarities in the Linker Region.[a]

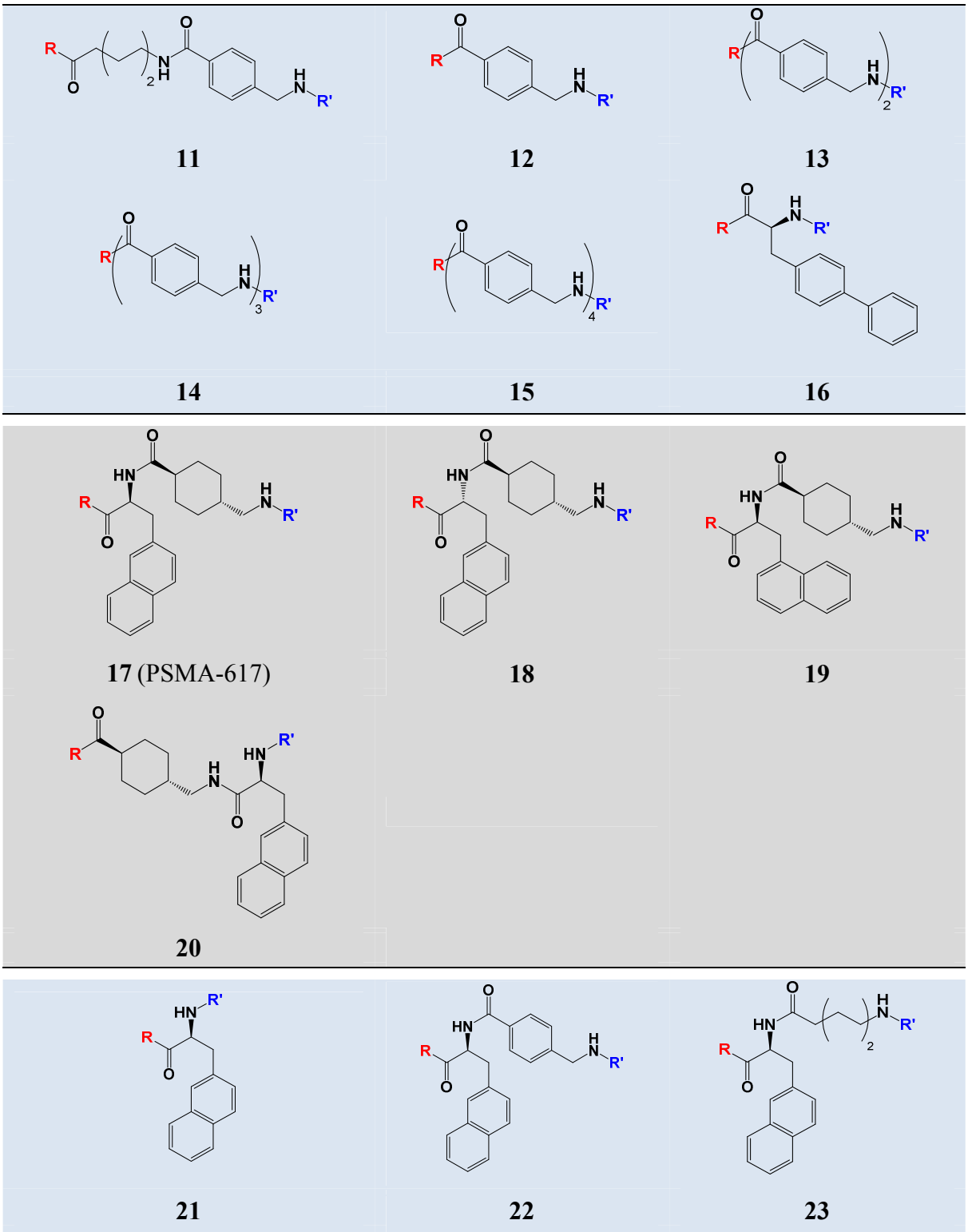

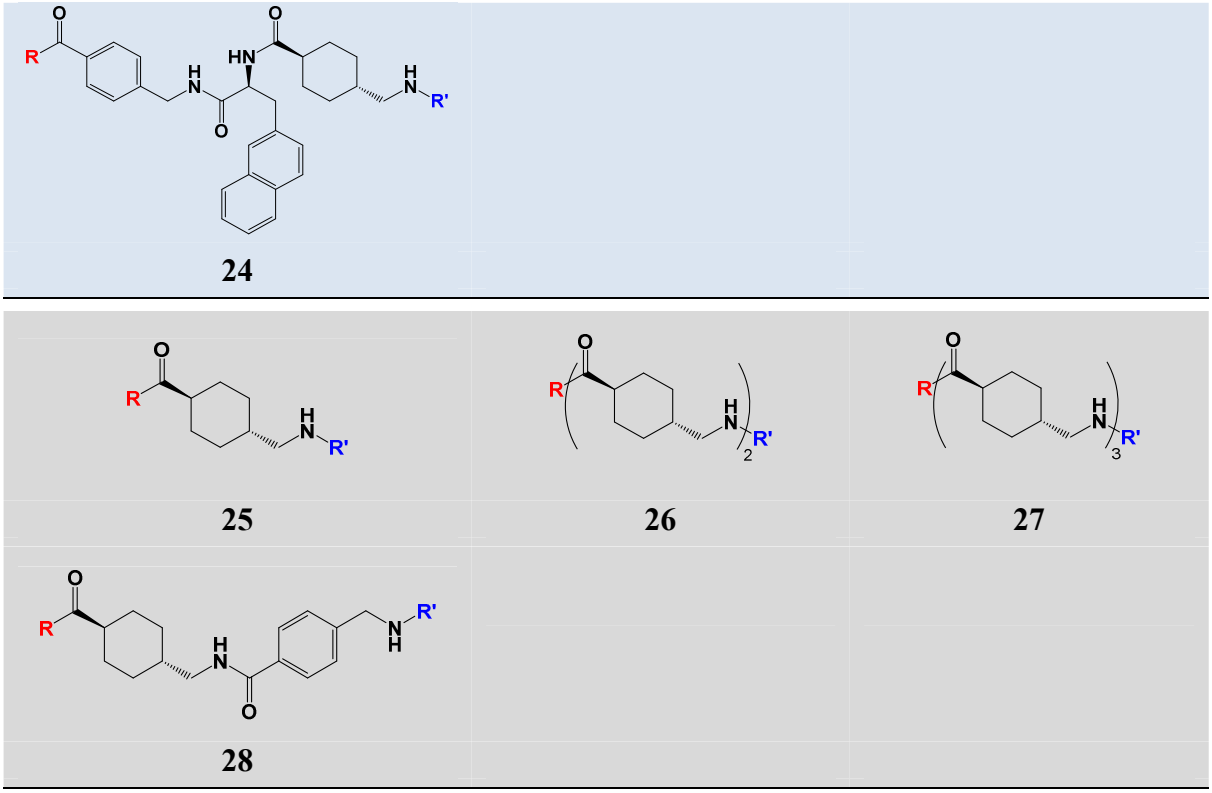

R = glutamate-urea-lysine binding motif; R' = DOTA chelator.

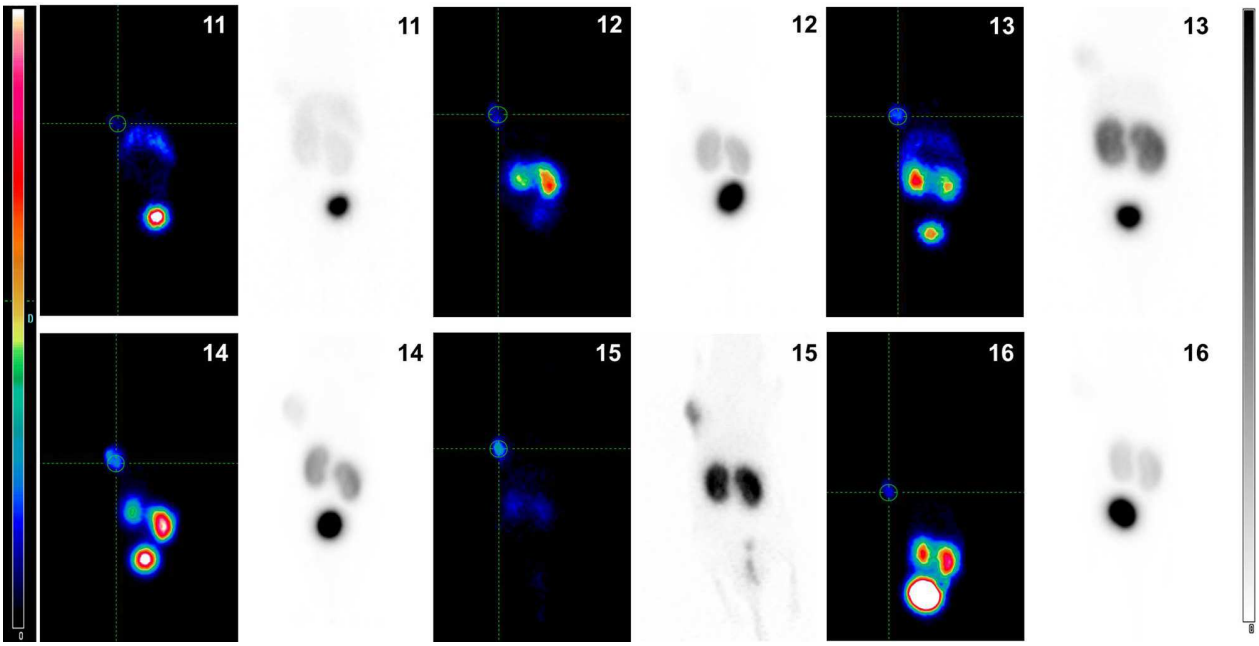

[a] The lacking visualization of the bladder for **15** was most probably caused by its emptying between 1 and 2 h.i.. In this time frame, the mouse was not anaesthetized.

Figure 3. Whole-body coronal slices (0.8 mm) (color) and MIPs (gray scale) derived from μPET imaging of an athymic nude mouse with LNCaP tumor (right trunk). Scans were evaluated up to 120 min post-injection of 0.5 nmol of ^{68}Ga-labeled (~30 MBq) **11**, **12**, **13**, **14**, **15**[a], and **16**.

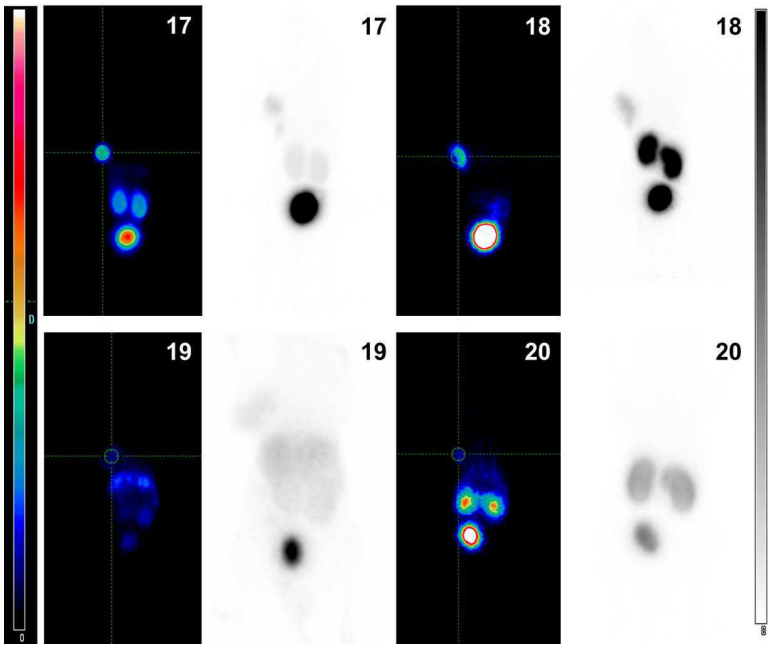

Figure 4. Whole-body coronal slices (0.8 mm) (color) and MIPs (gray scale) derived from μPET imaging of an athymic nude mouse with LNCaP tumor (right trunk). Scans were evaluated up to 120 min post-injection of 0.5 nmol of ^{68}Ga-labeled (~30 MBq) **17**, **18**, **19**, and **20**.

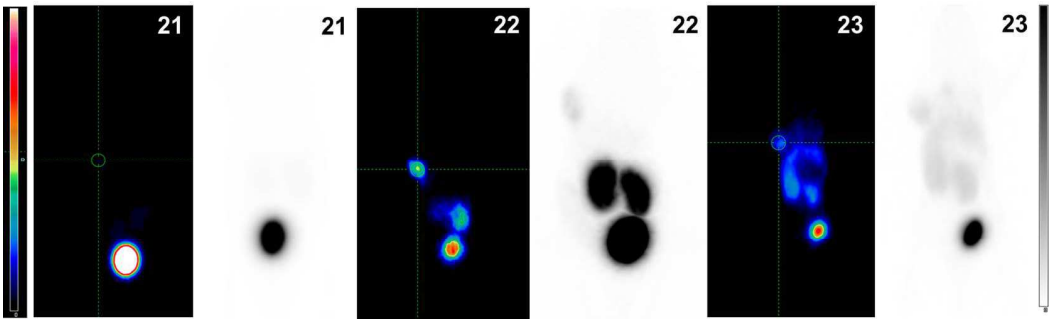

Figure 5. Whole-body coronal slices (0.8 mm) (color) and MIPs (gray scale) derived from μPET imaging of an athymic nude mouse with LNCaP tumor (right trunk). Scans were evaluated up to 120 min post-injection of 0.5 nmol of ^{68}Ga-labeled (~30 MBq) **21**, **22**, and **23**.

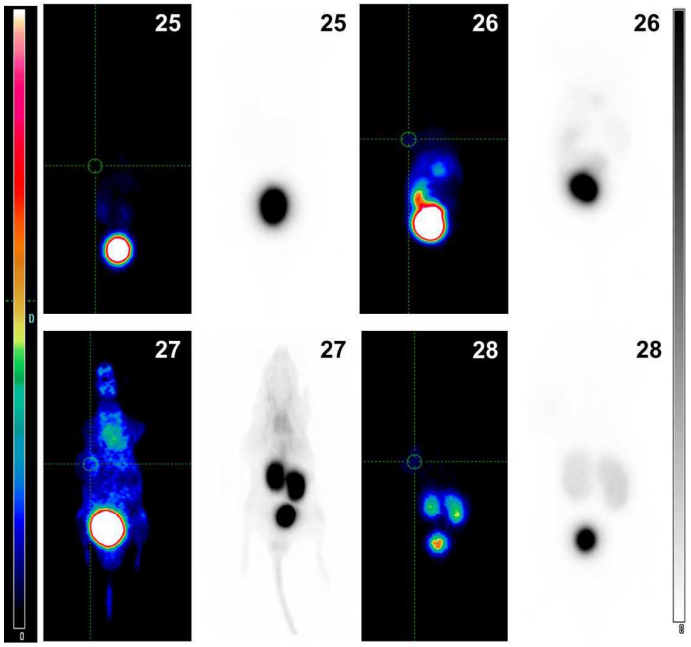

Figure 6. Whole-body coronal slices (0.8 mm) (color) and MIPs (gray scale) derived from μPET imaging of an athymic nude mouse with LNCaP tumor (right trunk). Scans were evaluated up to 120 min post-injection of 0.5 nmol of ^{68}Ga-labeled (~30 MBq) **25**, **26**, **27**, and **28**.

SCHEMES

Scheme 1. Synthesis of the Glutamate–Urea–Lysine Binding Motif

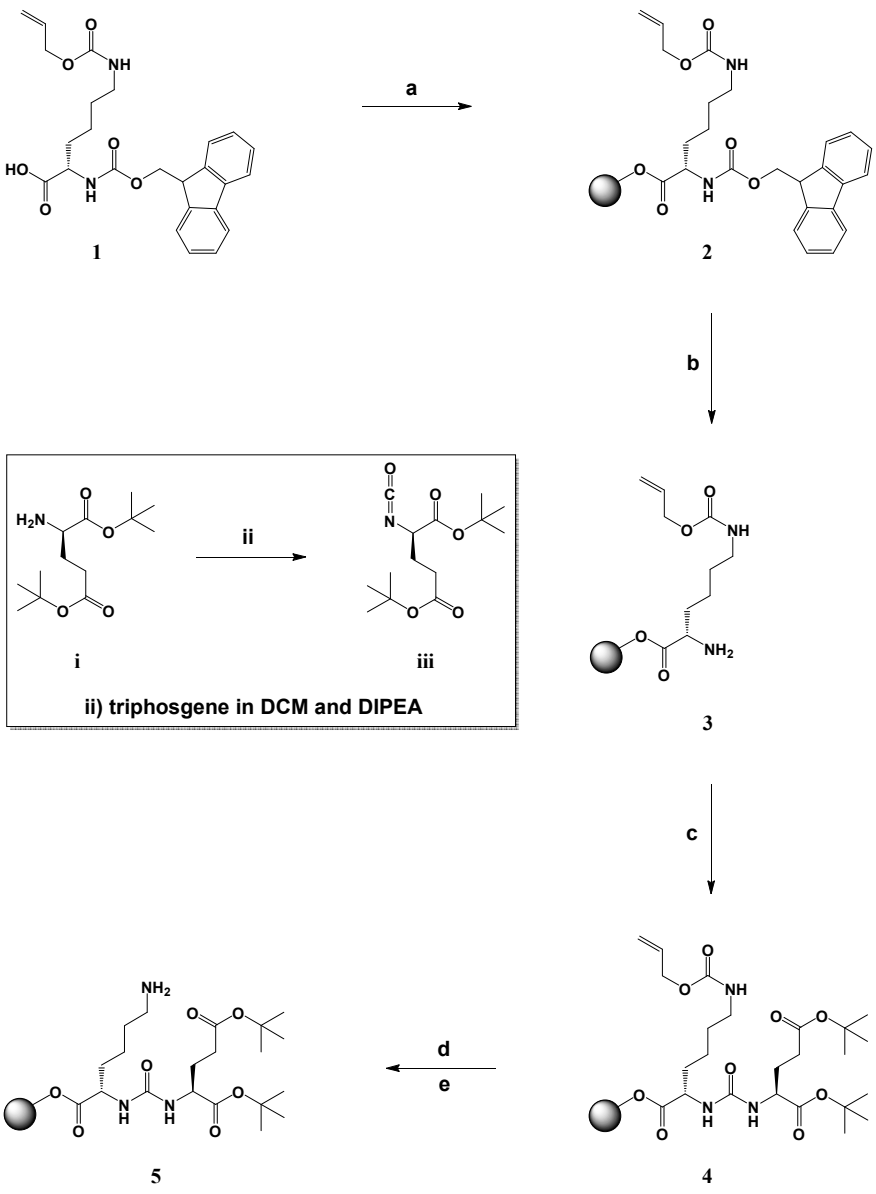

a) 2-CT-Resin in DCM and DIPEA; b) 50% piperidine in DMF; c) iii in DCM; d) TPP palladium in DCM and morpholine; e) 1% DIPEA in DMF, diethyldithiocarbamate in DMF

Scheme 2. Coupling of the Linker and Conjugation of the DOTA Chelator to Yield the Series of 18 PSMA Inhibitors

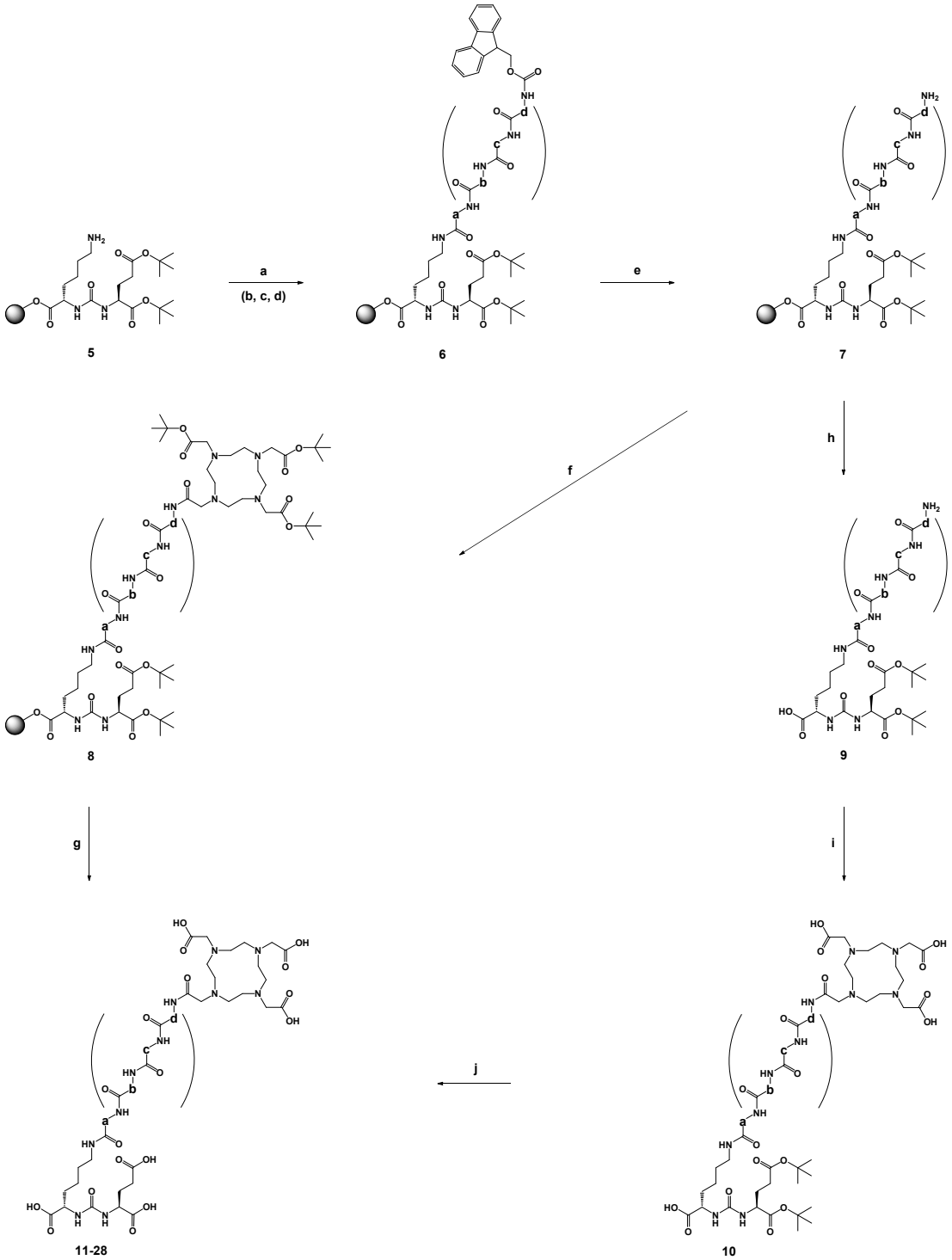

a) Fmoc-a-OH and HBTU in DMF and DIPEA; b) 50% piperidine in DMF, Fmoc-b-OH and HBTU in DMF and DIPEA; c) 50% piperidine in DMF, Fmoc-c-OH and HBTU in DMF and DIPEA; d) Fmoc-d-OH and HBTU in DMF and DIPEA; e) 50% piperidine in DMF; f) DOTA-tris(*t*Bu) ester and HBTU in DMF and DIPEA; g) TFA; h) HFIP in DCM; i) DOTA-NHS ester and HBTU in DMF and DIPEA; j) TFA

TABLES

Table 1. Analytical Data of Prepared Compounds

Compound code	MW [g/mol]	t_r[a] [min]	m/z[b]	log$D_{pH\ 7.4}$(exp) *n*-octanol/HEPES
29	947.00	1.69	947.4	−1.71 ± 0.62
11	952.04	1.74	953.0	−1.92 ± 0.20
12	838.88	1.56	839.9	−1.99 ± 0.04
13	972.03	1.78	972.7	−1.94 ± 0.21
14	1105.18	1.95	1106.0	−2.06 ± 0.17
15	1238.33	2.44	1239.1	−2.12 ± 0.33
16	929.00	2.59	929.6	−1.98 ± 0.19
17	1042.15	2.63	1042.9	−2.00 ± 0.31
18	1042.15	2.56	1042.6	−2.02 ± 0.08
19	1042.15	2.59	1042.7	−1.95 ± 0.05
20	1042.15	2.48	1042.8	−1.44 ± 0.07
21	902.96	2.71	903.6	−2.03 ± 0.14
22	1036.11	2.32	1036.6	−2.10 ± 0.06
23	1016.12	2.58	1016.7	−1.88 ± 0.26
24	1175.30	2.70	1176.1	n.d.
25	844.92	1.81	846.0	−0.91 ± 0.49
26	984.12	2.08	984.4	−1.12 ± 0.86
27	1123.31	2.28	1123.9	−1.98 ± 0.03
28	978.07	2.07	978.9	−1.43 ± 0.20

[a] Retention time of unlabeled ligand on analytical HPLC. [b] Mass spectrometry of the unlabeled ligand detected as $[M + H]^+$. n.d. = not determined, **24** demonstrated instability and degradation at higher temperatures and was thus neither tested *in vitro* nor *in vivo*.

Table 2. PSMA Inhibition Potencies[a] (expressed as K_i values) Determined with LNCaP Cells, Specific Cell Surface Binding, and Specific Internalization

Compound code	**Building blocks in linker area** (a-b-c-d)	K_i [nM]	**Specific cell surface binding** [%IA/10^6 cells]	**Specific internalization** [%IA/10^6 cells]
29	---	**12.0 ± 2.8**	**10.63 ± 2.93**	**9.47 ± 2.56**
11	Ahx, AMBA	15.31 ± 5.10	17.72 ± 2.18	2.11 ± 0.02
12	AMBA	1.97 ± 0.76	8.54 ± 5.34	5.11 ± 2.46
13	AMBA, AMBA	7.51 ± 6.12	14.29 ± 13.24	3.66 ± 1.31
14	**AMBA, AMBA AMBA**	**0.53 ± 0.47**	**21.43 ± 2.27**	**12.49 ± 1.38**
15	AMBA, AMBA AMBA, AMBA	6.19 ± 1.51	25.21 ± 10.98	6.86 ± 1.59
16	biphenyl-L-Ala	0.50 ± 0.63	4.93 ± 1.48	1.65 ± 0.44
17	**2-naphthyl-L-Ala AMCH**	**2.34 ± 2.94**	**11.40 ± 6.60**	**16.17 ± 3.66**
18	2-naphthyl-D-Ala AMCH	8.86 ± 3.64	12.25 ± 4.45	7.18 ± 3.47
19	1-naphthyl-L-Ala AMCH	12.78 ± 6.41	6.58 ± 2.46	0.90 ± 0.07
20	AMCH 2-naphthyl-L-Ala	17.70 ± 1.41	1.09 ± 0.06	0.13 ± 0.01
21	2-naphthyl-L-Ala	28.60 ± 13.10	1.68 ± 0.61	1.77 ± 1.19
22	**2-naphthyl-L-Ala AMBA**	**1.81 ± 0.80**	**16.77 ± 6.41**	**7.17 ± 2.82**
23	2-naphthyl-L-Ala Ahx	6.31 ± 2.22	9.07 ± 6.83	2.99 ± 1.65
24	AMBA 2-naphthyl-L-Ala AMCH	n.d.	n.d.	n.d.
25	AMCH	9.33 ± 28.39	4.14 ± 2.02	1.24 ± 0.24
26	AMCH, AMCH	20.96 ± 29.65	3.88 ± 5.49	1.43 ± 0.21
27	AMCH, AMCH	19.40 ± 5.18	0.23 ± 0.25	0.03 ± 0.02

	AMCH			
28	**AMCH, AMBA**	**24.71 ± 24.99**	**4.49 ± 5.79**	**2.70 ± 2.06**

N.b. The values for the most promising compound of each set, including the overall lead candidate, **17**, and reference compound, **29**, are highlighted in boldface type. [a] Data are expressed as means ± SD (n = 3). Ahx = 6-(Fmoc-amino)hexanoic acid; AMBA = 4-(Fmoc-aminomethyl)benzoic acid; AMCH = *trans*-4-(Fmoc-aminomethyl)cyclohexanecarboxylic acid; biphenyl-L-Ala = Fmoc-(4-biphenyl)-L-alanine; 2-naphthyl-L-Ala = Fmoc-(2-naphthyl)-L-alanine; 2-naphthyl-D-Ala = Fmoc-(2-naphthyl)-D-alanine; 1-naphthyl-L-Ala = Fmoc-(1-naphthyl)-L-alanine; n.d. = not determined, **24** demonstrated instability and degradation at higher temperatures and was thus neither tested *in vitro* nor *in vivo*.

Table 3. SUV_{mean} Values[a] for Tumor, Muscle, and Kidneys and T-to-B Ratios from μPET Imaging 1 h post-injection

^{68}Ga-Labeled compound	SUV tumor	SUV muscle	SUV kidneys	T-to-B ratio
29	n.d.	n.d.	n.d.	4.9
11	0.30 ± 0.09	0.08 ± 0.02	4.70 ± 1.37	3.8
12	0.28 ± 0.05	0.13 ± 0.04	2.68 ± 0.85	2.2
13	0.56 ± 0.13	0.10 ± 0.05	3.16 ± 1.13	5.6
14	**0.58 ± 0.20**	**0.11 ± 0.02**	**4.16 ± 1.81**	**5.4**
15	0.52 ± 0.13	0.25 ± 0.05	2.21 ± 0.71	2.1
16	0.63 ± 0.09	0.23 ± 0.05	6.57 ± 2.45	2.7
17	**0.59 ± 0.32**	**0.07 ± 0.02**	**2.87 ± 0.66**	**8.5**
18	0.69 ± 0.15	0.27 ± 0.05	3.98 ± 1.37	2.6
19	0.29 ± 0.07	0.08 ± 0.02	2.15 ± 0.52	3.6
20	0.39 ± 0.07	0.11 ± 0.03	3.62 ± 1.39	3.5
21	0.31 ± 0.06	0.20 ± 0.05	4.79 ± 2.66	1.6
22	**0.52 ± 0.26**	**0.10 ± 0.02**	**3.63 ± 1.78**	**5.2**
23	0.14 ± 0.10	0.07 ± 0.04	2.26 ± 0.62	2.0
24	n.d.	n.d.	n.d.	n.d.
25	0.23 ± 0.04	0.15 ± 0.03	6.86 ± 3.24	1.5
26	0.30 ± 0.10	0.13 ± 0.03	4.29 ± 1.39	2.3
27	0.18 ± 0.07	0.21 ± 0.05	2.91 ± 1.21	0.9
28	**0.54 ± 0.16**	**0.14 ± 0.04**	**8.10 ± 2.19**	**3.9**

N.b. The values for the most promising compound of each set, including the overall lead candidate, **17**, are highlighted in boldface type. [a] Data are expressed as means ± SD (n = 1). n.d.

= not determined, μPET imaging of **29** was not performed in SUV, **24** demonstrated instability and degradation at higher temperatures and was thus neither tested *in vitro* nor *in vivo*.

DISPLAYED EQUATIONS

Equation 1. Distribution coefficient (log*D*)

$$\log D_{\underset{\text{HEPES}}{\text{oct}}} = \frac{\log\left([solute]_{octanol}^{ionized} + [solute]_{octanol}^{unionized}\right)}{[solute]_{HEPES}^{ionized} + [solute]_{HEPES}^{unionized}}$$

where $\log D_{\text{oct/HEPES}}$ is the distribution coefficient between *n*-octanol and HEPES buffer (0.1 M HEPES, pH 7.4), $[solute]_{octanol}^{ionized}$ is concentration of ionized compound in the *n*-octanol phase, $[solute]_{octanol}^{unionized}$ is the concentration of unionized compound in the *n*-octanol phase, $[solute]_{HEPES}^{ionized}$ is the concentration of ionized compound in the HEPES phase, and $[solute]_{HEPES}^{unionized}$ is the concentration of unionized compound in the HEPES phase.

Equation 2. Conversion of IC_{50} to K_i[68]

$$K_i = IC_{50}\frac{1 + [c_{dimer}]}{K_d}$$

where K_i is the binding affinity of the inhibitor, $[c_{dimer}]$ is the fixed concentration of competitive ligand ^{68}Ga-**30** and K_d is the dissociation constant of ^{68}Ga-PSMA-**30**.

For Table of Contents Only